

The compressible vortex pair

By **D. W. MOORE**

Department of Mathematics, Imperial College, Queens Gate, London SW7 2BZ, UK

AND **D. I. PULLIN**

Department of Mechanical Engineering, University of Queensland, St. Lucia 4067, Australia

(Received 6 February 1987)

We consider the steady self-propagation with respect to the fluid at infinity of two equal symmetrically shaped vortices in a compressible fluid. Each vortex core is modelled by a region of stagnant constant-pressure fluid bounded by closed constant-pressure, constant-speed streamlines of unknown shape. The external flow is assumed to be irrotational inviscid isentropic flow of a perfect gas. The flow is therefore shock free but may be locally supersonic. The nonlinear free-boundary problem for the vortex-pair flow is formulated in the hodograph plane of compressible-flow theory, and a numerical solution method based on finite differences is described. Specific results are presented for a range of parameters which control the flow, namely the Mach number of the pair translational motion and the fluid speed on each vortex bounding streamline. Perturbation-theory predictions are developed, valid for vortices of small core radius when the pair Mach number is much less than unity. These are in good agreement with the hodograph-plane calculations. The numerical and the perturbation-theory results together confirm the recently discovered (Barsony-Nagy, Er-El & Yungster 1987) existence of continuous shock-free transonic compressible flows with embedded vortices. For the vortex-pair geometry studied, solution branches corresponding to physically acceptable flows that could be calculated using the present hodograph-plane numerical method were found to be terminated when either the flow on the streamline of symmetry separating the vortices tends to become superonic or when limiting lines appear in the hodograph plane giving a locally multivalued mapping to the physical plane.

1. Introduction and formulation

The importance of compressibility in the cores of concentrated vortices has been recognized for many years (Mack 1960; Brown 1965; Küchemann 1978, p. 368) and compressibility effects are present in numerical calculations of vortices in supersonic flow past an inclined cone (Marconi 1985). Recent experimental studies using pulsed laser holographic interferometry (Mandella, Moon & Bershader 1986) indicate that vortices produced in a compressible fluid by shock diffraction at the end of a channel may have supersonic flow in the core region, and that the core pressure can be less than 30% of the pressure at the outer edge of the vortex.

There has, however, been little theoretical work specifically on the interaction of vortices in a compressible fluid, although, of course, such interactions are present, among many other effects, in the numerical study cited. An exception is the thin vortex ring, whose self-induced velocity in a compressible fluid was calculated by Moore (1985). The effect of compressibility on the ring velocity proved to be of the

order of the square of the Mach number of the circulatory motion in the core. For a ring of fixed dimensions and circulation the self-induced velocity decreased as the Mach number increased.

In plane incompressible flow the analogue of a vortex ring is a pair of vortices with circulations of equal magnitude and opposite sense. If the circulation is Γ (primed symbols denote dimensional variables and unprimed symbols denote their dimensionless equivalents), and the cores are small and separated by a distance $2D'$, the pair advances steadily at a speed $\Gamma/4\pi D'$. Thus the flow is steady in suitably translating axes.

Our objective is to study this flow in an inviscid compressible fluid, using primarily numerical methods so that we are not restricted to small core sizes or small compressibility effects. For these latter cases we employ a perturbation method due to Barsony-Nagy, Er-El & Yungster (1987).

The flow outside the cores will be taken to be irrotational and isentropic and it remains to specify the conditions within the cores. For simplicity, we insist that the fluid within the cores is stagnant, so that the core boundaries are curves on which the pressure, or equivalently, the fluid speed is constant. We denote this constant value by q'_v .

An upper bound on the possible values of q'_v is provided by the requirement that the core pressure be non-negative. Thus $q'_v \leq q'_{ev}$ where

$$q'_{ev} = \left(\frac{\gamma + 1}{\gamma - 1} \right)^{\frac{1}{2}} c^{*'}, \quad (1.1)$$

and $c^{*'}$ denotes the sound speed at the sonic point. If $\gamma = 1.4$, which we assume throughout, $q'_{ev} = 2.45\dots c^{*'}$, so that the flow field can contain extensive regions of supersonic flow if the assigned value of q'_v is sufficiently large. Thus our numerical method must be able to deal with transonic flow.

We define $2D'$ to be the separation between the centres of vorticity of the cores. Then the physical quantities determining the flow are Γ' , D' , q'_v , c'_∞ and ρ'_∞ , where c'_∞ is the sound speed at infinity and ρ'_∞ the fluid density at infinity. Given these quantities, we must find a flow field with velocity potential $\phi'(x', y')$ such that the core boundaries are both streamlines and constant-pressure lines and

$$\phi' \sim -q'_\infty x' \quad \text{as } x'^2 + y'^2 \rightarrow \infty, \quad (1.2)$$

where q'_∞ is the velocity of advance of the pair.

We are assuming a steady flow to exist in axes $Ox'y'$ fixed in the vortex pair; specifically, the vorticity centroids are at $(0, D')$ and $(0, -D')$, the core at $(0, D')$ having circulation Γ' and that at $(0, -D')$ circulation $-\Gamma'$.

We shall go on to impose reflectional symmetry of the core boundaries in both axes. However, we do not assert there are no other solutions, because experience with free-boundary problems has shown that less symmetric steady solutions can bifurcate off solutions of obvious symmetry (e.g. Chen & Saffman 1980 for the Stokes wave case). Perturbation theory suggests that this symmetry is the only possibility for small cores, but the question of other solutions remains open, because our numerical method cannot detect the relevant bifurcations.

Dimensional analysis shows that

$$P = \frac{4\pi D' q'_\infty}{\Gamma'} = f\left(\frac{D' q'_v}{\Gamma'}, \frac{\Gamma'}{D' c'_\infty}\right) \quad (1.3)$$

so that we have a two-parameter family of solutions to deal with. When $\Gamma/D'c'_\infty = 0$, the flow field is incompressible and was determined by Pocklington (1894) by using Kirchhoff's free-streamline theory. Although our detailed procedure uses different non-dimensionalization we have, in essence, been able to start with a known solution for a chosen value of the first parameter, which is a measure of the size of the vortex, and then increase the second, which is a Mach number $M_r = \Gamma/D'c'_\infty$, from zero.

The fact that the flow speed is known on the internal boundaries suggests that the problem can be conveniently formulated in the hodograph plane. We consider this in the following section.

Our assumption that the flow field exterior to the cores is isentropic and irrotational implies that there are no shock waves. Since the flow field contains stagnation points, it is likely that a shock-free flow exists only if $M_\infty = q'_\infty/c'_\infty < 1$. We have imposed this condition in our detailed formulation.

2. The hodograph plane

2.1. Non-dimensionalization

We now dimensionalize by writing

$$x' = L'x, \quad y' = L'y, \quad t' = T't, \quad (2.1)$$

where t' is the time and, for the density $\rho'(x', y')$,

$$\rho' = M' L'^{-3} \rho, \quad (2.2)$$

where unprimed quantities are non-dimensional. An unusual feature of the problem is that a convenient choice of the length, time and mass scales L' , T' and M' is not at this stage apparent. This is because our work will be done in the hodograph plane, and D' and Γ' are thus not available as basic scales at the outset. We are however free to choose $\rho_\infty = 1$, so we have

$$L'^3 \rho'_\infty M'^{-1} = 1 \quad (2.3)$$

as one relation between our scales.

2.2. The flow in the hodograph plane

When we impose reflectional symmetry in both axes the flow field and boundary shapes need be determined only in the $\frac{1}{4}$ -plane $x, y \geq 0$. Thus we have the configuration sketched in figure 1.

We introduce a velocity potential $\phi(x, y)$ and a stream function $\psi(x, y)$ such that the velocity field $(u(x, y), v(x, y))$ is given by

$$u = \frac{\partial \phi}{\partial x} = \rho^{-1} \frac{\partial \psi}{\partial y}, \quad v = \frac{\partial \phi}{\partial y} = -\rho^{-1} \frac{\partial \psi}{\partial x}, \quad (2.4)$$

from which it follows that (Milne-Thomson 1966, §15.44)

$$dz = \frac{e^{i\theta}}{q} \left(d\phi + i \frac{d\psi}{\rho} \right), \quad (2.5)$$

where $z = x + iy$, and $u - iv = q e^{-i\theta}$, so that

$$\frac{\partial z}{\partial q} = \frac{e^{i\theta}}{q} \left(\frac{\partial \phi}{\partial q} + i \frac{\partial \psi}{\rho \partial q} \right), \quad (2.6)$$

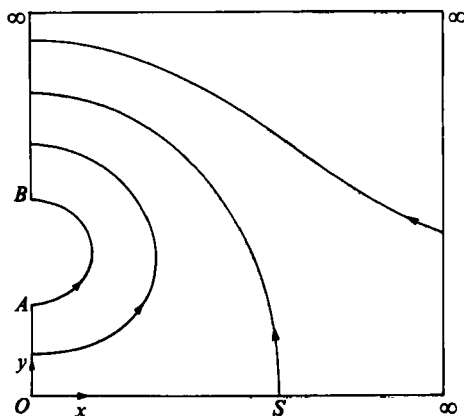


FIGURE 1. The physical plane showing some typical streamlines. *S* is the stagnation point and *AB* the vortex core boundary. The complete flow pattern can be obtained by reflections *Ox* and *Oy*.

and

$$\frac{\partial z}{\partial \theta} = \frac{e^{i\theta}}{q} \left(\frac{\partial \phi}{\partial \theta} + \frac{i}{\rho} \frac{\partial \psi}{\partial \theta} \right). \tag{2.7}$$

Compatibility of these equations gives

$$\frac{\partial \phi}{\partial q} = q \frac{\partial \psi}{\partial \theta} \frac{\partial}{\partial q} \left(\frac{1}{\rho q} \right) \tag{2.8}$$

and

$$\frac{\partial \phi}{\partial \theta} = \frac{q}{\rho} \frac{\partial \psi}{\partial q}. \tag{2.9}$$

We also have Bernoulli's theorem

$$\frac{1}{2}q^2 + \frac{c^2}{\gamma - 1} = \frac{c_s^2}{\gamma - 1} \tag{2.10}$$

and the isentropic flow relation

$$\frac{c^2}{c_\infty^2} = \rho^{\gamma - 1}, \tag{2.11}$$

where $c(x, y)$ is the local sound speed and c_s the stagnation sound speed. Elimination of ϕ from (2.8) and (2.9) and use of (2.10) and (2.11) leads to the equation

$$q^2 \left(1 - \frac{q^2(\gamma - 1)}{2c_s^2} \right) \frac{\partial^2 \psi}{\partial q^2} + q \left(1 - \frac{q^2(\gamma - 3)}{2c_s^2} \right) \frac{\partial \psi}{\partial q} + \left(1 - \frac{q^2(\gamma + 1)}{2c_s^2} \right) \frac{\partial^2 \psi}{\partial \theta^2} = 0, \tag{2.12}$$

which we shall write, for brevity, $\mathcal{L}(\psi) = 0$. This is the governing equation for the flow in the (q, θ) or hodograph plane.

Next we must determine the image in the hodograph plane of the boundary $AB \infty SO$ (figure 1) of the flow region in physical space. Starting at O where $q = q_0$, we note that on OA , $\theta = 0$; on AB , $q = q_v$, which is prescribed, and on $B \infty$, $\theta = \pi$. At ∞ , $\theta = \pi$ and $q = q_\infty$; on ∞S , $\theta = \pi$; at S , $q = 0$ and $0 \leq \theta \leq \pi$ and on SO , $\theta = 0$. Thus, as sketched in figure 2, the flow domain in the hodograph plane is the rectangle

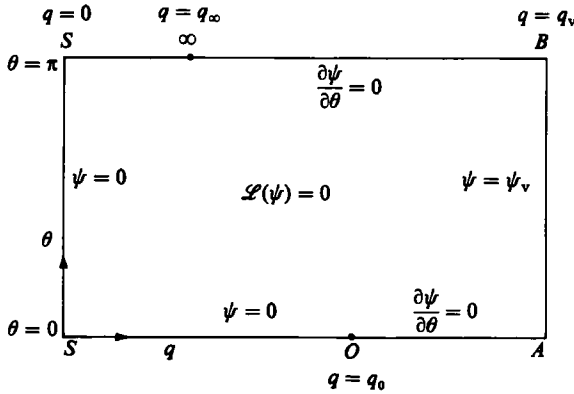


FIGURE 2. The hodograph-plane formulation. \mathcal{L} is the differential operator defined in (2.12). The point ∞ is at (q_∞, π) while O is at $(q_0, 0)$ where q_0 is unknown.

$0 \leq q \leq q_v, 0 \leq \theta \leq \pi$. We note that the mapping between the physical plane and the hodograph plane must be singular on the boundary of the flow domain, because the hodograph image of the point S is the interval $q = 0, 0 \leq \theta \leq \pi$. We shall deal with the effect of this singularity in due course.

It remains to find the boundary values of ψ in the hodograph plane. We choose $\psi = 0$ on the axis of symmetry ∞SO and $\psi = \psi_v$ on the vortex boundary AB . The boundary condition on OA or $B\infty$ is derived by noting that on these lines $\partial x / \partial q = 0$, while $\theta = 0$ on OA and $\theta = \pi$ on $B\infty$. Thus (2.6) gives $\partial \phi / \partial q = 0$ so that (2.8) gives $\partial \psi / \partial \theta = 0$.

We are thus led to the formulation of the problem in the hodograph plane sketched in figure 2. The crucial point is that, unlike the case of flow past obstacle of prescribed shape, the physical boundary conditions yield a complete specification of the hodograph-plane problem. Thus the principal difficulty traditionally associated with the hodograph method disappears. It is this, rather than the linearity of \mathcal{L} , which makes the hodograph-plane method viable. We have, however, to pay a price for this reduction of the original free-boundary-value problem, because we are restricted to streamlines on which θ lies between O and π . Thus, in particular, the vortex-core boundary cannot develop a waist at AB , because this would involve values of θ less than zero and greater than π . It will later be shown that this restricts solutions that can be obtained with the present method to those for which the local Mach number $M_0 = q_0/c_0$ at O satisfies $M_0 < 1$.

We now examine the hodograph-plane formulation in more detail. First we note that the parameters q_0 and ψ_v are unknown. Secondly we observe the change in type of the boundary condition on ψ at the points $(q_0, 0)$ and (q_∞, π) . This switch will cause ψ to have singularities at these points and we must determine the form and strength of these singularities by examination of the flow in the physical plane. We note that for solutions with a hodograph of this form $q_0 < q_v$.

2.3. The singularities at ∞ and at 0

We choose to examine the nature of the singularities first. As remarked in §1, we assume that the flow at ∞ is subsonic, since a shock-free flow field seems unlikely otherwise. Then the flow at large distances from the pair is a uniform stream $(-q_\infty, 0)$ plus a small perturbation, whose form can be found from the subsonic version of

linearized-flow theory. Introducing the appropriate Mach number $M_\infty = q_\infty/c_\infty$, we find that the velocity potential is

$$\phi = -q_\infty x - \frac{\lambda x}{x^2 + (1 - M_\infty^2) y^2}, \tag{2.13}$$

where the second term is a dipole of strength λ , distorted by the Prandtl–Glauert transformation, with unknown strength and with orientation determined by the reflectional symmetry. To leading order (recalling that $\rho_\infty = 1$), the stream function is given by

$$\psi = -q_\infty y, \tag{2.14}$$

while the velocity field is given by

$$u = -q_\infty - \frac{\lambda((1 - M_\infty^2) y^2 - x^2)}{(x^2 + (1 - M_\infty^2) y^2)^2} \tag{2.15}$$

and

$$v = \frac{2\lambda xy(1 - M_\infty^2)}{(x^2 + (1 - M_\infty^2) y^2)^2}; \tag{2.16}$$

note that (2.16) shows $\lambda > 0$ since $v > 0$ from figure 1. If we eliminate x and y from (2.14), (2.15) and (2.16) we find that, to leading order,

$$\psi \sim A s^{-\frac{1}{2}} \cos \frac{1}{2} \delta, \tag{2.17}$$

where local quasi-polar coordinates in the hodograph plane are defined by

$$s e^{i\delta} = \frac{q - q_\infty}{q_\infty} + i \frac{(\theta - \pi)}{(1 - M_\infty^2)^{\frac{1}{2}}}; \tag{2.18}$$

the constant A is given by

$$A = -q_\infty^{\frac{1}{2}} \lambda^{\frac{1}{2}} (1 - M_\infty^2)^{-\frac{1}{2}}. \tag{2.19}$$

This singular behaviour is worse than might have been anticipated. For the Laplace operator (to which \mathcal{L} reduces near $(q_\infty, 0)$ after a Prandtl–Glauert stretching) conformal mapping shows that the natural singularity at a change of type is

$$\psi \sim B s^{\frac{1}{2}} \cos \frac{1}{2} \delta. \tag{2.20}$$

Thus the principle of ‘minimum singularity’ fails here and we must find a way to impose the behaviour (2.17). We can show (Appendix A) that

$$\psi \sim \psi_s + B s^{\frac{1}{2}} \cos \frac{1}{2} \delta + O(s^{\frac{3}{2}}) \quad \text{as } (q, \theta) \rightarrow (q_\infty, \pi), \tag{2.21}$$

where

$$\psi_s = A(s^{-\frac{1}{2}} \cos \frac{1}{2} \delta + s^{\frac{1}{2}}(B_1 \cos \frac{3}{2} \delta + B_2 \cos \frac{7}{2} \delta)), \tag{2.22}$$

where B_1 and B_2 are known and B is unknown. We now write

$$\psi = \hat{\psi} + \psi_s \tag{2.23}$$

and solve

$$\mathcal{L}(\hat{\psi}) = -\mathcal{L}(\psi_s), \tag{2.24}$$

subject to modified boundary conditions and the requirement that $\hat{\psi}$ has singular behaviour of type (2.20) at (q_∞, π) and – as is shown by local analysis in the physical

plane – at $(q_0, 0)$ also, provided that $M_0 < 1$. Our method of implementing this requirement will be described in §4.

Clearly A is a fundamental constant of the problem and we complete our specification of scales by imposing $A = -1$ and $q_\infty = 1$. Thus

$$q'_\infty T' L'^{-1} = 1, A' L'^{-2} T' = -1, \quad (2.25)$$

so that (2.3) and (2.25) fix L', T' and M' in terms of the physical quantities ρ'_∞, q'_∞ and λ' . In conformity with our convention A' and λ' are the dimensional quantities whose dimensionless forms are A and λ . The characterisation of the pair by the quantities q'_∞ and λ' rather than D' and Γ is unusual, but is forced on us by our method of solution. For a vortex pair with very small cores in an incompressible fluid

$$q'_\infty = \frac{\Gamma}{4\pi D'} \quad (2.26)$$

and

$$\lambda' = \frac{\Gamma D'}{\pi}, \quad (2.27)$$

so that Γ and D' are easily determined from q'_∞ and λ' in this case. Also, for this case $q_0 = 3q_\infty$.

We must at this point refer to a potentially serious difficulty, which is that we do not know if the solution of the above boundary-value problem is unique. Since the boundary-value problem is linear, this is equivalent to asking if the homogeneous problem obtained by setting $A = \psi_v = 0$ has a non-zero solution. The difficulty is in the transonic case where the eigensolutions correspond to stationary sound waves trapped in the recirculating region near the vortex. Indeed, sound waves of infinitesimal amplitude can be trapped in the potential vortex, recirculating flow around the exterior of a rigid circular cylinder if the Mach number based on the cylinder diameter takes certain critical values (Taylor 1930).

If eigensolutions exist at critical values of M_∞ , our non-homogeneous problem would have no solution at these critical values. Near such an eigenvalue our problem would be ill-posed and the solution would vary rapidly with M_∞ . We shall consider this question again in §5 when we examine our results.

2.4. The unknowns q_0 and ψ_v

We now return to what is the sole remaining problem in determining $\psi(q, \theta)$, namely that q_0 and ψ_v are not known and must be determined as part of the solution.

First, we note that because of the singularity in the mapping at S , imposition of the boundary condition $\psi = 0$ on $q = 0$ is insufficient to ensure the correct behaviour of ψ as $q \rightarrow 0$. Near the stagnation point the effect of compressibility can be neglected and

$$\psi \sim exy, \quad (2.28)$$

so that

$$\rho_0 u \sim ex \quad (2.29)$$

and

$$\rho_0 v \sim -ey, \quad (2.30)$$

where ρ_0 is the stagnation density and e is a constant. Hence, as $q \rightarrow 0$ we must have

$$\psi \sim -\frac{\rho_0^2}{2e} q^2 \sin 2\theta. \quad (2.31)$$

Now the full equation has, for $q < 1$, the exact solution

$$\psi(q, \theta) = \sum_1^{\infty} G_n(q) \sin n\theta \quad (0 \leq \theta \leq \pi), \quad (2.32)$$

where $G_n(q) \sim g_n q^n$ as $q \rightarrow 0$. Comparison with (2.31) shows that the $n = 1$ term must be absent from the expansion (2.32), which is satisfied if

$$I_1(q_0, \psi_v; q_1) \equiv \int_0^{\pi} \psi(q_1, \theta) \sin \theta \, d\theta = 0 \quad (2.33)$$

for any q_1 such that $0 < q_1 < 1$.

Secondly, we remark that the image in the physical plane of the line segment $q = q_2$, $0 \leq \theta \leq \pi$, must begin and end at $x = 0$ (i.e. $x_A = x_B$ in figure 1) for every q_2 such that $q_0 < q_2 \leq q_v$. Use of (2.5) and (2.9) gives

$$I_2(q_0, \psi_v; q_2) \equiv \frac{1}{\rho} \int_0^{\pi} \left(\cos \theta \frac{\partial \psi}{\partial q} - \frac{\sin \theta}{q} \frac{\partial \psi}{\partial \theta} \right) \Big|_{q=q_2} d\theta = 0 \quad (2.34)$$

and it is easy to show from the separated solution that this holds for all q_2 in the interval if it holds for one.

3. Constructing the physical plane

The numerical procedure to be described in §4 yields the unknown parameters q_0 and ψ_v and the stream function $\psi(q, \theta)$. In this brief section we consider the construction of the physical plane sketched in figure 1.

Suppose l is a curve in the (q, θ) -plane defined by the equations

$$\frac{dq}{d\mu} = \cos [\Theta(q, \theta)], \quad (3.1)$$

$$\frac{d\theta}{d\mu} = \sin [\Theta(q, \theta)]. \quad (3.2)$$

where μ is the arclength on the curve and Θ is the angle between the local tangent to l in the direction of increasing μ and the q -axis. The curve l might be $q = \text{constant}$, in which case $\Theta = \pm \frac{1}{2}\pi$, or $\theta = \text{constant}$, with $\Theta = 0, -\pi$, or l might be a streamline when

$$\cos [\Theta(q, \theta)] = \frac{\psi_{\theta}}{(\psi_q^2 + \psi_{\theta}^2)^{\frac{1}{2}}}, \quad (3.3)$$

$$\sin [\Theta(q, \theta)] = \frac{-\psi_q}{(\psi_q^2 + \psi_{\theta}^2)^{\frac{1}{2}}}. \quad (3.4)$$

Then the complex representation $z(\mu)$ of the image of l in the physical plane satisfies

$$\frac{dz}{d\mu} = \frac{\partial z}{\partial q} \frac{dq}{d\mu} + \frac{\partial z}{\partial \theta} \frac{d\theta}{d\mu}, \quad (3.5)$$

which leads to

$$\frac{dz}{d\mu} = \frac{e^{i\theta}}{q} \left[\left(q \frac{\partial\psi}{\partial\theta} \frac{\partial}{\partial q} \left(\frac{1}{\rho q} \right) + \frac{i}{\rho} \frac{\partial\psi}{\partial q} \right) \cos \Theta + \left(\frac{q}{\rho} \frac{\partial\psi}{\partial q} + \frac{i}{\rho} \frac{\partial\psi}{\partial\theta} \right) \sin \Theta \right], \quad (3.6)$$

in view of (2.6)–(2.0). Equations (3.1), (3.2) and (3.6) constitute a real fourth-order autonomous system to determine $x(\mu)$, $y(\mu)$, $q(\mu)$ and $\theta(\mu)$, given $x(0)$, $y(0)$, $q(0)$ and $\theta(0)$ say.

The physical plane image of l given by $(x(\mu), y(\mu))$ will – in general – exhibit cuspidal behaviour if $dz/d\mu$ has a simple zero. This will happen if

$$q \frac{\partial\psi}{\partial\theta} \frac{\partial}{\partial q} \left(\frac{1}{\rho q} \right) \cos \Theta + \frac{q}{\rho} \frac{\partial\psi}{\partial q} \sin \Theta = 0 \quad (3.7)$$

and
$$\frac{1}{\rho} \frac{\partial\psi}{\partial q} \cos \Theta + \frac{1}{\rho} \frac{\partial\psi}{\partial\theta} \sin \Theta = 0. \quad (3.8)$$

Now $\cos \Theta$ and $\sin \Theta$ cannot simultaneously vanish. Thus a necessary condition for cuspidal behaviour is

$$\begin{vmatrix} q \frac{\partial\psi}{\partial\theta} \frac{\partial}{\partial q} \left(\frac{1}{\rho q} \right), & \frac{q}{\rho} \frac{\partial\psi}{\partial q} \\ \frac{1}{\rho} \frac{\partial\psi}{\partial q}, & \frac{1}{\rho} \frac{\partial\psi}{\partial\theta} \end{vmatrix} = 0, \quad (3.9)$$

leading to
$$\Delta = -\frac{q}{\rho^2} \left[\left(\frac{\partial\psi}{\partial q} \right)^2 + \frac{1}{q^2} \left(\frac{\partial\delta}{\partial\theta} \right)^2 \left(1 - \frac{q^2}{c^2} \right) \right] = 0, \quad (3.10)$$

where c is the local sound speed.

From a standard result,

$$\Delta = q^2 \frac{\partial(x, y)}{\partial(q, \theta)}, \quad (3.11)$$

so that (Landau & Lifschitz 1959, p. 432) a necessary condition for the success of the hodograph method is that

$$\frac{\partial(x, y)}{\partial(q, \theta)} < 0. \quad (3.12)$$

We monitored the values of Δ obtained numerically and rejected any solutions in which regions of positive Δ developed. Another result which tests the consistency of the results is Nikolskii & Taganov's theorem (Landau & Lifschitz 1959) which states that the velocity vector rotates monotonically on the sonic line.

4. Numerical method

4.1. Numerical method

A direct finite-difference numerical solution of (2.24) on a uniform grid in the (q, θ) -plane proved impractical for several reasons. First, large values of q_v for some cases would then require unrealistically large numbers of grid points to achieve resolution. Secondly, we decided that in order to reduce errors it was desirable to fix the singular

point $q_\infty = 1$, and the (variable) singular point $q = q_0$ at or near a cell centre. Hence prior to differencing we utilized a simple univariate stretching in the θ -direction, and an adaptive local stretching in the q -direction of the form

$$\theta = \theta(\eta), \quad \theta(0) = 0, \quad \theta(\pi) = \pi, \quad (4.1)$$

$$q = q(\xi), \quad q(0) = 0, \quad q(1) = q_v. \quad (4.2)$$

Under the stretchings (4.1–4.2), (2.24) becomes

$$E(\xi) \frac{\partial^2 \hat{\psi}}{\partial \xi^2} + F(\xi) \frac{\partial \hat{\psi}}{\partial \xi} + G(\xi) H_1(\eta) \frac{\partial^2 \hat{\psi}}{\partial \eta^2} + G(\xi) H_2(\eta) \frac{\partial \hat{\psi}}{\partial \eta} = -\mathcal{L}[\hat{\psi}_s(\xi, \eta)], \quad (4.3)$$

where

$$\left. \begin{aligned} E(\xi) &= q^2 \left[1 - \frac{q^2(\gamma-1)}{2c_s^2} \right] \left(\frac{d\xi}{dq} \right)^2, \\ F(\xi) &= q^2 \left[1 - \frac{q^2(\gamma-1)}{2c_s^2} \right] \frac{d^2 \xi}{dq^2} + q \left[1 - \frac{q^2(\gamma-3)}{2c_s^2} \right] \frac{d\xi}{dq}, \\ G(\xi) H_1(\eta) &= \left[1 - \frac{q^2(\gamma+1)}{2c_s^2} \right] \left(\frac{d\eta}{d\theta} \right)^2, \\ G(\xi) H_2(\eta) &= \left[1 - \frac{q^2(\gamma+1)}{2c_s^2} \right] \frac{d^2 \eta}{d\theta^2}, \end{aligned} \right\} \quad (4.4)$$

subject to the boundary conditions, obtained from figure 2 and (2.23),

$$\left. \begin{aligned} S-\infty: \quad & \hat{\psi} = 0, \\ \infty-B: \quad & \hat{\psi}_\eta = 0, \\ B-A: \quad & \hat{\psi} = \psi_v - \psi_s(1, \eta) \\ A-0: \quad & \hat{\psi}_\eta = -\frac{(\psi_s)_\theta}{\eta_\theta} \\ 0-S: \quad & \hat{\psi} = -\psi_s(\xi, 0), \\ S-S: \quad & \hat{\psi} = -\psi_s(0, \eta), \end{aligned} \right\} \quad (4.5)$$

and $\psi_s = \psi_s[q(\xi), \theta(\eta)]$ is given by (2.22).

When $q_v < q_{ev}$ we have a two-parameter (q_v, M_∞) problem which we shall refer to as the compressible Poklington (1894) vortex (CPV). When $q_v = q_{ev}$ we reach a singular limit of the CPV where the vortex pressure is zero. Here $q_{ev} = q_{ev}(M_\infty)$ (see (5.4)) and we have a one-parameter (M_∞) problem which we shall refer to as the evacuated vortex (EV). In either case, for fixed parameters, the method of numerical solution adopted presently divides into two parts: an inner algorithm where the linear problem (4.1)–(4.5) is solved numerically for fixed q_0, ψ_v , and an outer algorithm where q_0 and ψ_v are determined by Newton iteration on the (2×2) nonlinear problem given by (2.33)–(2.34). We first describe the inner algorithm.

4.2. The inner problem: the finite difference method

The mixed elliptic ($0 < q < c^*$)–hyperbolic ($c^* < q < q_v$) equation (4.3) was solved numerically using second-order central differences on a fixed grid

$$\left. \begin{aligned} \xi_j &= j \Delta \xi, & j &= 0 \dots J, \\ \eta_i &= i \Delta \eta, & i &= 0 \dots I, \end{aligned} \right\} \quad (4.6)$$

where $\Delta \xi = 1/J$, $\Delta \eta = \pi/I$, and we put $\hat{\psi}_{ji} = \hat{\psi}(\xi_j, \eta_i)$. Specific forms of (4.1)–(4.2) were chosen as

$$\theta(\eta) = \eta - \epsilon_\theta \sin(2\eta), \quad (4.7)$$

$$q(\xi) = -\frac{q_v}{\alpha_q} \log [1 - \xi(1 - e^{-\alpha_q})] + \epsilon_q \sin \left[\frac{2\pi(1 - e^{-\beta\xi})}{1 - e^{-\beta}} \right]. \quad (4.8)$$

Equation (4.7) concentrates cells near $\theta = 0, \pi$ when $\epsilon_\theta > 0$. If $\epsilon_q = 0$, (4.8) reduces the cell density near $q = q_v$ when $\alpha_q > 0$. If ϵ_q is small, the amount of stretching is nearly the same but the formula can be tuned to ensure that $\xi(q_\infty)$ and $\xi(q_0)$ lie at cell centres.

In practice, values of α_q , ϵ_q and β were calculated as follows: first an estimate of α_q based on the desired amount of stretching was specified in the outer algorithm. Next ϵ_q was set equal to zero and $\hat{\xi}_0$ and $\hat{\xi}_\infty$ computed from the requirements that $q(\hat{\xi}_0) = q_0$ and $q(\hat{\xi}_\infty) = 1$. The points $\hat{\xi}_0$ and $\hat{\xi}_\infty$ will not be at cell centres, but we can define ξ_0 and ξ_∞ to be the coordinates of the closest cell centres, so for some integers j_0 and j_∞ ,

$$\xi_0 = (j_0 - \frac{1}{2}) \Delta \xi, \quad \xi_\infty = (j_\infty - \frac{1}{2}) \Delta \xi. \quad (4.9)$$

Next the parameter β was determined from

$$\frac{2(1 - \exp(-\frac{1}{2}\beta(\xi_0 + \xi_\infty)))}{1 - \exp(-\beta)} = 1, \quad (4.10)$$

which ensures that the second term in (4.8) has different signs at $\xi = \xi_\infty$ and $\xi = \xi_0$; we found this restriction desirable. Once calculated, ξ_∞ , ξ_0 and β remain fixed throughout the computation of the outer problem. For each solution of the inner problem, α_q and ϵ_q were then found by requiring

$$q(\xi_\infty; \alpha_q, \epsilon_q) = 1, \quad q(\xi_0; \alpha_q, \epsilon_q) = q_0. \quad (4.11)$$

This adaptive q -stretching ensured that $q_\infty = 1$ and $q = q_0$ always remained near† cell centres while maintaining overall local stretching corresponding approximately to the prechosen α_q . Variations of α_q were $O(\Delta \xi)$ and ϵ_q was always $O(\Delta \xi)$.

The discrete solution domain \mathcal{D} consists of all grid points (j, i) at which $\hat{\psi}_{ji}$ is unknown. Thus, because of the switch in boundary conditions, \mathcal{D} increases in height as j increases through the switch values j_∞ and j_0 ; the upper step at j_∞ is shown in detail in figure 3. We obtain linear equations for the unknowns $\hat{\psi}_{ji}$ by insisting that the finite-difference form of (4.3) holds at each point of \mathcal{D} . We must next explain how we deal with the boundary points of D where the stencil protrudes from \mathcal{D} .

Implementation of the Dirichlet boundary conditions in (4.5) was straightforward. For the Neumann boundary conditions, ghost points outside \mathcal{D} were defined at

$$\left. \begin{aligned} \eta_{-1} &= -\Delta \eta, & \xi_j &= j \Delta \xi, & j &= j_0 \dots J-1, \\ \eta_{I+1} &= (I+1) \Delta \eta, & \xi_j &= j \Delta \xi, & j &= j_\infty \dots J-1. \end{aligned} \right\} \quad (4.12)$$

† Near, not exactly, because we solved (4.11) approximately.

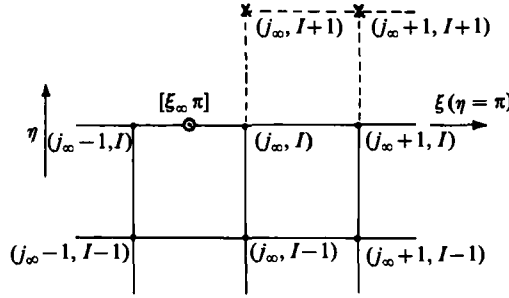


FIGURE 3. Finite-difference grid near singularity at $\odot = [\xi_\infty, \pi]$ in the $[\xi, \eta]$ -plane. \bullet , grid point; \times , ghost point.

The $\hat{\psi}_j$ of these points are easily expressed in terms of their mirror-image values from the symmetry properties of ψ . Second-order difference forms of (4.3), and also of the derivative boundary conditions in (5.4) were then applied at

$$\left. \begin{aligned} \eta_0 = 0, \quad \xi_j = j \Delta \xi, \quad j = j_0 \dots J-1, \\ \eta_I = \pi, \quad \xi_j = j \Delta \xi, \quad j = j_\infty \dots J-1. \end{aligned} \right\} \quad (4.13)$$

The residual unforced $s^{\frac{1}{2}}$ singular behaviour (see (2.20) and Appendix A) for $\hat{\psi}$ near $(q, \theta) = (1, \pi)$ and for ψ near $(q, \theta) = (q_0, \pi)$ was injected onto the difference grid in the simplest possible way. Assuming that (2.20) is valid locally within the cell containing $(\xi, \eta) = (\xi_\infty, \pi)$ on its boundary in figure 3, a linear relationship between $\hat{\psi}_{j_\infty, I}$ and $\hat{\psi}_{j_\infty, I-1}$ containing known coefficients is easily found. This was then used to eliminate $\hat{\psi}_{j_\infty, I}$ when the difference stencil was applied at $(j, i) = (j_\infty + 1, I)$ and at $(j, i) = (j_\infty, I-1)$. A similar scheme was used to eliminate $\hat{\psi}_{j_0, 0}$ near $(q, \theta) = (q_0, 0)$. We note that the injection of unforced singular terms i.e. those containing unknown constants as in A 11) to $O(s^{\frac{1}{2}})$ only may lead to errors in $\hat{\psi}$ near the singularities of $O(h^{\frac{1}{2}})$, $h = \Delta \xi$ or $\Delta \eta$. Some improvement may be expected by use of a local expansion to higher order than that given in Appendix A. However, the coupling of higher-order terms into the difference grid in a rational way substantially increases the bandwidth of the resulting linear equation system.

For known (q_0, ψ_v) , the boundary-value problem now reduces to $(J-1)(I+1) - (j_\infty + j_0)$ linear equations for an equal number of unknowns. The use of central differences in the hyperbolic as well as in the elliptic subdomain will generally preclude the successful iterative solution of the linear equation system. Although the use of upwind differences in the hyperbolic subdomain may allow iterative solution, this was rejected in favour of uniform central differences and a direct method because of our desire to eliminate uncertainties from the novel hodograph-plane problem. Numbering the $\hat{\psi}_j$ i -wise then gave a bandwidth of $2I+3$. The linear system was solved in 14-figure arithmetic using a vectorized banded solver kindly supplied by Dr B. Fornberg.

4.3. The outer problem

Once the ψ_j are known the integrals in (2.33) and (2.34) may be evaluated. This was done using central differences for the derivatives, and the periodic trapezoidal rule for the integrals, after using symmetry to extend the integration range to $(0, 2\pi)$. Equation (2.34) was evaluated on $i = 2$. For the CPV, (2.35) was evaluated on

$j = J - 2$ while for the EV a special form of (2.35) was used (see (4.20)). The outer problem may then be written as

$$I_1(q_0, \psi_v; q_1) = 0, \quad I_2(q_0, \psi_v; q_2) = 0; \quad (4.14a, b)$$

that is, two equations for two unknowns q_0 and ψ_v .

This was solved by Newton iteration, evaluating the Jacobian by central differences thus requiring 5 solutions of the inner problem per outer iteration. Convergence of the outer problem was accepted subject to

$$|I_k| \leq 10^{-10}, \quad k = 1, 2$$

and $\Delta < 0$ (equation (3.10)) in the solution domain.

Starting values of q_0 and ψ_v for the CPV cases were obtained from the Pocklington theory valid for $M_\infty = 0$. Then as M_∞ was increased in steps at fixed q_v , previous converged values of q_0 and ψ_v were used to extrapolate as M_∞ was increased in steps at fixed q_v ; previous converged values of q_0 and ψ_v were used to extrapolate starting values. For the EV case we obtained analytic estimates for q_0 (equation (6.10)) and ψ_v (equation (B 10)) valid in the limit of core radius $R' \ll D'$, equivalent to $M_\infty \ll 1$; these values were used to start the Newton iteration at the smallest value of M_∞ considered.

4.4. Special procedure for the EV

For the EV computations, some special treatment of the inner problem was required owing to the singular behaviour of $\psi(q, \theta)$, $q \rightarrow q_{ev}$. For $q > q_0$, $q_v = q_{ev}$, it may be shown that the solution of (2.12) which satisfies the boundary conditions of figure 2 and which has the required behaviour when $q \rightarrow q_{ev}$ can be written as a separated solution of the form

$$\psi = \psi_v + \sum_{n=0}^{\infty} D_n \cos(n\theta) \tau^{\frac{1}{2}n} (1-\tau)^{\frac{\gamma}{2}} F(c-b, c-a, c-a-b+1, 1-\tau), \quad (4.15)$$

$$\left. \begin{aligned} c &= n+1, \\ \left. \begin{aligned} (a) &= \frac{1}{2} \left\{ n - \frac{1}{\gamma-1} \pm \left[\left(\frac{\gamma+1}{\gamma-1} \right) n^2 + \frac{1}{(\gamma-1)^2} \right]^{\frac{1}{2}} \right\}, \\ (b) &= \frac{1}{2} \left\{ n - \frac{1}{\gamma-1} \mp \left[\left(\frac{\gamma+1}{\gamma-1} \right) n^2 + \frac{1}{(\gamma-1)^2} \right]^{\frac{1}{2}} \right\}, \end{aligned} \right\} \\ \tau &= \left(\frac{q}{q_{ev}} \right)^2, \end{aligned} \right\} \quad (4.16)$$

where F is the hypergeometric function, and D_n , $n = 0 \dots$, are unknown coefficients. Together with the density equation for $q_v = q_{ev}$,

$$\rho = \left[\frac{1}{2}(\gamma-1) M_\infty^2 (q_{ev}^2 - q^2) \right]^{\frac{1}{\gamma-1}}, \quad (4.17)$$

(4.15) may be used to show that (2.34) is satisfied automatically when $D_1 = 0$.

Expanding the hypergeometric functions in (4.15) in powers of $1-\tau$ shows that

$$\psi = \psi_v + (q_v - q)^{\frac{\gamma}{2}} [E_1(\theta) + E_2(\theta)(q_v - q) + E_3(\theta)(q_v - q)^2 + O(q_v - q)^3], \quad (4.18)$$

where the $E_s(\theta)$, $s = (1, 2, 3)$ are unknown functions of θ only. Hence when $\gamma = 1.4$, ψ is weakly singular as $(q_v - q)^{3.5}$ when $q \rightarrow q_{ev}$. The use of second-order differences in $\xi(q)$ near $\xi = 1$ ($q = q_{ev}$) assumes however that ψ is locally well represented by a second-order polynomial, and this was found to give irregular behaviour for ψ near

the vortex boundary. A more appropriate difference approximation was thus obtained by assuming a local three-term solution of form (4.18) centred on $q = q_j$, $J - J_{\text{ev}} \leq j < J - 1$, and a local two-term solution (neglecting E_3) near q_{j-1} ($q_j = q_{\text{ev}}$). The q -derivatives in (2.12) were then evaluated in terms of the unknowns $E_s(\theta_i)$, $i = 0 \dots I$ at each j . These latter quantities may easily be expressed as linear combinations of $\hat{\psi}_{j-1,i}$, $\hat{\psi}_{j,i}$, $\hat{\psi}_{j+1,i}$ using (4.18) and (2.23). Using centred differences for $\psi_{\theta\theta}$ in (2.12) then gives a special stencil for use at gridpoints $j = J - J_{\text{ev}} \dots J - 1$, $i = 0 \dots I$, which preserves the singular behaviour of ψ near the vortex. For the outer problem (2.34) (also (4.14b)) reduces to

$$I_2(q_0, \psi_v; q_{\text{ev}}) = \int_0^\pi E_1(\theta) \cos \theta d\theta. \quad (4.19)$$

Once $E_1(\theta)$ is known, computation of the vortex boundary shape in the physical plane is straightforward. Here we used $J_{\text{ev}} = 4$ or 8 depending on the values of q_{ev} and the grid size ($J \times I$).

5. Results

5.1. Range of parameters

For the most part the CPV computations discussed here were calculated on each of two finite-difference grids with $(J \times I) = (76 \times 20)$ and (150×40) respectively. Owing to the very large values of $q_{\text{ev}} (= O(10^2))$ for the EV, grids of size $(J \times I) = (300 \times 40)$ and (600×30) were used. The only input required was M_∞ , q_v and α_θ together with estimates of the target α_q . Where overall stretching was not required, $(\alpha_q, \alpha_\theta) = (O(h), 0)$ were used. With $q_v = 2.5$ and 3.0, the smallest values used here $(\alpha_q, \alpha_\theta) \approx (-3, 0.3)$ and $(\alpha_q, \alpha_\theta) \approx (-1, 0.2)$, respectively, were chosen since here $q_0 \rightarrow q_v$ so that the region between the x -axis of symmetry and the vortex bottom boundary near A in figure 1 becomes nearly singular in the (q, θ) -plane (e.g. note the regions of large θ -derivative in figure 6). When $q_v > 10$ for the CPV and for all EV computations, $3 \lesssim \alpha_q \lesssim 8$.

Generally results are presented with the scale specification $q_\infty = 1$, $A = -1$ (see (2.25)) but constructions of the physical plane will usually have $q_\infty = 1$, $\Gamma = 2\pi$. Transformation between these scales simply requires length rescaling by $\Gamma/2\pi$. All calculations presented have $\gamma = 1.4$.

5.2. Test of the numerical method

When $M_\infty = 0$, the CPV computations recover the single-parameter (q_v) family of solutions corresponding to the hollow-core vortex pair in an incompressible fluid studied by Pocklington (1894). As a check on the present method a comparison between the important physical parameters of these solutions and those obtained from the present method when $M_\infty = 0$ is given in table 1. The numerical evaluation of the incompressible Pocklington solutions are accurate to better than $O(10^{-6})$. There is substantial three-figure agreement between these solutions and the present hodograph-plane solutions, with $(J \times J) = (150 \times 40)$, for most quantities, which is consistent with expectation of errors $O(h)^2$ from use of second differences for both the field equation and the boundary conditions. An exception is the prediction of q_0 . This quantity, which is about equal to 3 ($q_0 = 3$ exactly for the incompressible point-vortex pair), always exhibits errors which increase with increasing q_v to $O(1\%)$ for $q_v = 10$ and $q_v = 20$. When $q_v \gg 1$, fewer grid points in the q -direction are

$J \times I$	q_v	α	q_0	ψ_v	Area	y_A	y_B	Γ
76 × 20	2.5	-2.994	2.420	0.4808	0.4942	0.1962	0.7675	6.693
150 × 40	2.5	-2.998	2.424	0.4846	0.4990	0.1976	0.7715	6.735
Pocklington	2.5	—	2.4269	0.48773	0.50264	0.19882	0.77478	6.7619
76 × 20	3	-0.997	2.697	0.6405	0.3457	0.2288	0.7626	6.472
150 × 40	3	-0.994	2.687	0.6404	0.3505	0.2289	0.7599	6.532
Pocklington	3	—	2.6910	0.64045	0.34906	0.22889	0.75864	6.512
76 × 20	5	0.083	2.985	1.119	0.1260	0.3147	0.6845	6.310
150 × 40	5	0.066	2.973	1.118	0.1258	0.3147	0.6838	6.315
Pocklington	5	—	2.9592	1.1173	0.12592	0.31485	0.68355	6.3140
76 × 20	10	-0.086	3.073	1.804	0.0313	0.4007	0.5968	6.262
150 × 40	10	0.073	3.035	1.802	0.0313	0.4011	0.5969	6.274
Pocklington	10	—	2.9976	1.8032	0.03144	0.40194	0.59802	6.2851
150 × 40	20	2.897	3.040	2.494	0.00758	0.4494	0.5483	6.242
Pocklington	20	—	3.0000	2.4961	0.00793	0.45022	0.54968	6.2833

TABLE 1. Comparison of numerical solution for the incompressible Pocklington vortex with present hodograph-plane numerical solutions, $M_\infty = 0$. Values of $J \times I$ shown. $q_\infty = 1$, $A = 1$.

concentrated near $q_\infty = 1$ and $q = q_0$. Use of $\alpha \approx 2.9$ for $q_v = 20$ stretches the q -variable in this region but also introduces derivatives of large magnitude into error terms neglected in second-order differencing. Also it may be expected that predictions of q_0 will be sensitive to possible errors of $O(h)^{\frac{1}{2}}$ in ψ near $(q, \theta) = (q_0, 0)$ owing to our crude treatment of the $O(s^{\frac{1}{2}})$ singularity described in §4. The presence of this singularity and of the equivalent one for $\hat{\psi}$ near $(q, \theta) = (1, \pi)$ renders a formal error analysis difficult and none has been attempted.

5.3. The CPV results

The parameter space for the CPV calculations are summarized in figure 4 and in tables 2–6. In the tables a is one half of the maximum x -dimension of each vortex and $b = 0.5(y_B - y_A)$ (figure 1). Hence b/a is a measure of the ellipticity of the vortex core. Specific examples of streamlines in the (q, θ) - and (x, y) -planes are shown in figures 6–11.

Figure 5 shows an example of the finite-difference grid mapped into the physical plane. This was obtained by integrating (3.1), (3.2) and (3.6) along lines $q(\xi) = \text{constant}$ in the (ξ, η) -plane using a fourth-order Runge-Kutta method with step size $\Delta\mu = \frac{1}{2}\Delta\eta$ near $(q, \theta) = (q_0, 0)$ and $\Delta\mu = \Delta\eta$ elsewhere. The required initial conditions $x(0), y(0)$ in the physical plane were first found by integration along $\eta = 0$ from the (x, y) -origin O . An analytical integration based on the local form of ψ given by (2.20) near O was used for the first step. Near $q = 0$ in the (q, θ) -plane a four-term expansion of the type (2.32) was used in which the G_n were determined from the numerical solution for ψ by integration on $J = 4$. Note in figure 5 the very large deformation of the finite-difference cell containing O produced by the square-root singularity in the $(q, \theta) \rightarrow (x, y)$ mapping.

CPV computations were performed by incrementing M_∞ from zero while q_v is held constant. At sufficiently large M_∞ , the local Mach number on the vortex boundary $M_v = q_v/c_v$, given by

$$M_v^2 = \frac{M_\infty^2 q_v^2}{1 + \frac{1}{2}(\gamma - 1) M_\infty^2 (1 - q_v^2)}, \quad (5.1)$$

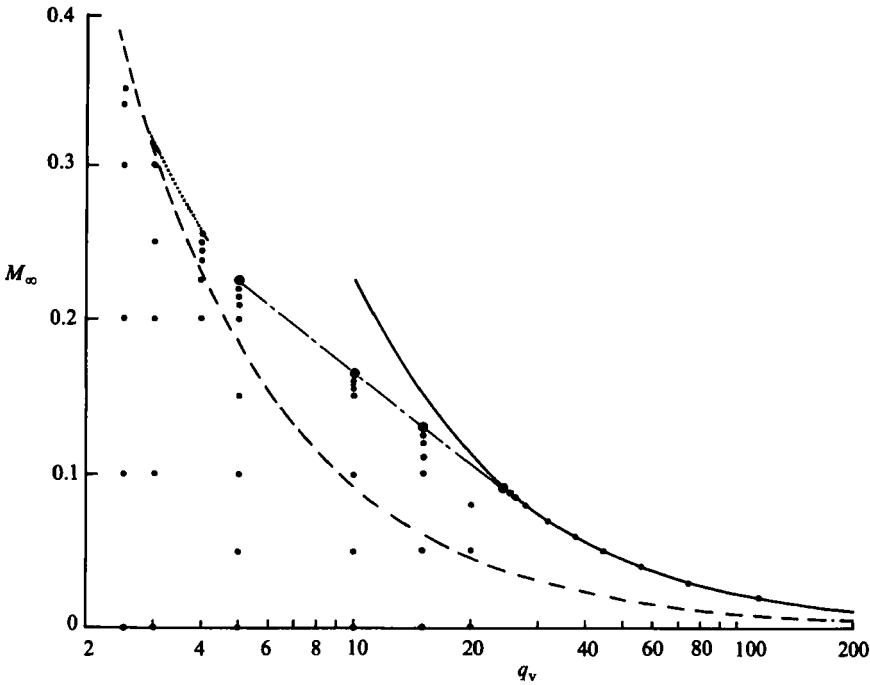


FIGURE 4. Summary of parameter space and limitations imposed by solution characteristics. ●, computed point; —, evacuated vortex (equation (5.2)); ----, $M_v = 1.0$ (equation (5.1)), $M_0 \approx 0.96$; - · - · - ·, $\Delta > 0$ encountered in (q, θ) -plane.

$J \times I$	M_∞	q_0	M_0	M_v	ψ_v	D	Area	a/b	Γ
150×40	0	2.424	0	0	0.485	0.462	0.499	1.87	6.74
76×20	0.10	{2.425 2.430}	{0.244 0.244}	0.2513	{0.470 0.473}	0.455	0.487	1.91	6.67
150×40									
76×20	0.20	{2.440 2.448}	{0.498 0.500}	0.5108	{0.436 0.439}	0.439	0.464	2.01	6.59
150×40									
76×20	0.30	{2.46 2.47}	{0.773 0.776}	0.7882	{0.383 0.384}	0.413	0.4246	2.22	6.46
150×40									
76×20	0.35	{2.46 2.48}	{0.922 0.928}	0.9374	{0.350 0.354}	0.395	0.395	2.39	6.37
150×40									
76×20	0.36	{2.47 2.48}	{0.952 0.959}	0.9683	{0.343 0.347}	0.391	0.389	2.44	6.35
150×40									

TABLE 2. Calculated properties for the compressible Pocklington vortex (CPV) pair. $q_v = 2.5$. Values of M_∞ as shown. $q_\infty = 1$, $A = -1$.

goes sonic. The curve $M_v = 1$ is shown in figure 4. On increasing M_∞ further, a limiting value is reached where ρ_v and p_v both vanish. This corresponds to the EV where $q_v = q_{ev}$. This limiting M_∞ , the maximum possible value corresponding to the fixed q_v , is given by

$$\frac{1}{M_\infty^2} = \frac{1}{2}(\gamma - 1)(q_{ev}^2 - 1) \tag{5.2}$$

and this curve is also shown on figure 4.

$J \times I$	M_∞	q_0	M_0	M_v	ψ_v	D	Area	a/b	Γ
150 × 40	0	2.69	0	0	0.640	0.482	0.351	1.56	6.53
76 × 20 150 × 40	0.10	{2.72 2.71}	{0.273 0.273}	0.3024	{0.614 0.617}	{0.472 0.475}	{0.340 0.342}	{1.59 1.58}	{6.44 6.47}
76 × 20 150 × 40		{2.778 2.779}	{0.571 0.571}		{0.560 0.563}	{0.457 0.459}	{0.324 0.325}	{1.69 1.68}	{6.36 6.38}
76 × 20 150 × 40	0.30	{2.89 2.91}	{0.926 0.933}	0.9728	{0.476 0.480}	{0.431 0.433}	{0.294 0.294}	{1.94 1.92}	{6.23 6.24}
76 × 20 150 × 40		{2.88 2.92}	{0.964 0.980}		{0.467 0.470}	{0.428 0.430}	{0.289 0.290}	{1.97 1.96}	{6.21 6.22}

TABLE 3. As table 2, $q_v = 3.0$.

$J \times I$	M_∞	q_0	M_0	M_v	ψ_v	D	Area	a/b	Γ
150 × 40	0	2.97	0	0	1.119	0.498	0.1258	1.182	6.315
76 × 20 150 × 40	0.1	{3.03 3.02}	{0.306 0.305}	0.5125	{1.059 1.058}	{0.494 0.493}	{0.1241 0.1239}	{1.199 1.198}	{6.270 6.275}
76 × 20 150 × 40		{3.11 3.10}	{0.476 0.474}		{0.987 0.986}	{0.489 0.488}	{0.1215 0.1213}	{1.237 1.237}	{6.220 6.224}
76 × 20 150 × 40	0.20	{3.26 3.25}	{0.679 0.676}	1.112	{0.893 0.892}	{0.482 0.481}	{0.1173 0.1171}	{1.312 1.313}	{6.146 6.150}
76 × 20 150 × 40		{3.32 3.30}	{0.730 0.726}		{0.872 0.871}	{0.480 0.480}	{0.1162 0.1160}	{1.335 1.336}	{6.129 6.132}
76 × 20 150 × 40	0.220	{3.41 3.43}	{0.791 0.798}	1.255	{0.850 0.849}	{0.479 0.478}	{0.1150 0.1147}	{1.363 1.364}	{6.111 6.113}

TABLE 4. As table 2, $q_v = 5.0$.

$J \times I$	M_∞	q_0	M_0	M_v	ψ_v	D	Area	a/b	Γ
150 × 40	0	3.03	0	0	1.803	0.4989	0.03134	1.041	6.274
76 × 20 150 × 40	0.05	{3.09 3.05}	{0.155 0.153}	0.5129	{1.743 1.740}	{0.4980 0.4979}	{0.03122 0.03121}	{1.047 1.047}	{6.253 6.262}
76 × 20 150 × 40		{3.14 3.10}	{0.316 0.313}		{1.572 1.569}	{0.4952 0.4952}	{0.03082 0.03084}	{1.071 1.071}	{6.22 6.23}
76 × 20 150 × 40	0.15	{3.25 3.21}	{0.498 0.492}	2.014	{1.330 1.328}	{0.4910 0.4908}	{0.02988 0.02994}	{1.147 1.155}	{6.15 6.16}
76 × 20 150 × 40		{3.27 3.25}	{0.542 0.540}		{1.257 1.263}	{0.4899 0.4891}	{0.02900 0.02935}	{1.221 1.227}	{6.14 6.15}

TABLE 5. As table 2, $q_v = 10$.

$J \times I$	M_∞	q_0	M_0	M_v	ψ_v	D	Area	a/b	Γ
150 × 40	0	3.04	0	0	2.49	0.499	0.0075	1.010	6.24
150 × 40	0.05	3.06	0.153	1.118	2.26	0.498	0.0078	1.017	6.25
150 × 40	0.08	3.07	0.247	2.287	1.966	0.494	0.0072	1.049	5.94

TABLE 6. As table 2, $q_v = 20$.

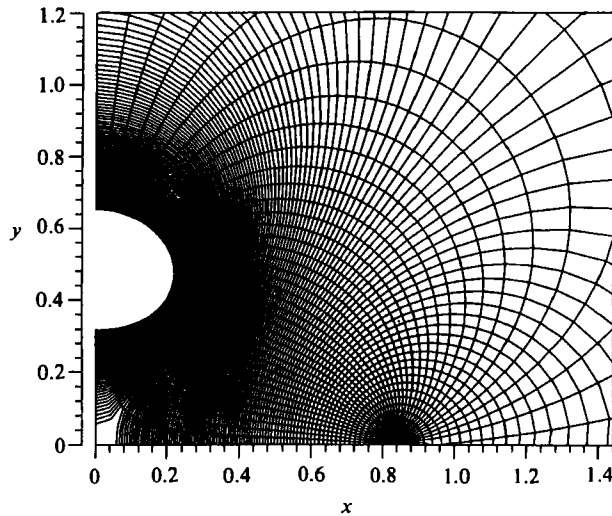


FIGURE 5. Finite-difference grid in the physical plane, $q_v = 5$, $M_\infty = 0.20$; $q_\infty = 1$, $\Gamma = 2\pi$. Lines of $q(\xi) = \text{const}$ and $\theta(\eta) = \text{const}$ shown. $(J \times I) = (150 \times 40)$.

We now discuss the characteristics of the CPV numerical solutions for $2.5 \leq q_v \leq 20$, the approach for M_∞ increasing (at constant q_v) of physically acceptable CPV solutions towards the EV limit was found to be terminated by the appearance of effects which are summarized in figure 4. It has already been noted that the present hodograph formulation is restricted to solutions for which the flow at O is locally subsonic, i.e. $M_0 < 1.0$. This is because we have a locally subsonic solution of the type (2.20) near O built into the finite-difference structure. It might be thought possible to replace (2.20) by a locally transonic approximation valid near $(q, \theta) = (q_0, 0)$ when $M_0 > 1$. This is not so, since under the assumed (x, y) -symmetry properties of the solution in the physical plane, it is easy to show, assuming the one-dimensional theory holds approximately, that the limiting streamtube bounded by $y = 0$ must then have an area *maximum* at $x = 0$, and this would require $\theta < 0$ near O , which is not consistent with the hodograph restriction $0 \leq \theta \leq \pi$. With $q_v = 2.5, 3$ and 4 respectively we found that our solutions were indeed terminated when $M_0 \rightarrow 1$. When $q_v = 2.5$ we found we could not proceed past $M_0 = 0.96$ at $M_\infty = 0.360$ (table 2); when $q_v = 3$ we were stopped at $M_0 = 0.98$ where $M_\infty = 0.310$ (table 3); while when $q_v = 4$ we were stopped at $M_0 \approx 0.98$ at $M_\infty = 0.260$ (not tabulated). As $M_0 \rightarrow 1$, the streamlines in the (x, y) -plane between the vortex-boundary bottom at A in figure 1 and O becomes flattened, and the flow approaches a uniform nearly sonic channel flow as illustrated in figure 7(b). In the (q, θ) -plane, q_0 then approaches q_v (see tables 2 and 3) and ψ becomes nearly singular on $\theta = 0$, $q_0 < q \leq q_v$. This may be seen in figure 6 ($M_0 \approx 0.93$) where the streamlines converge on the grid scale near $(q, \theta) = (q_v, 0)$. There is also some non-smoothness of the streamlines in figure 6 near $\theta = 0$. This is possibly the effect of the $O(s^{\frac{1}{2}})$ singularity at $(q, \theta) = (q_0, 0)$. This local irregularity always occurred in varying degrees near O and was generally confined to this region. The streamlines in the (x, y) -plane for the case of figure 6(b) shown in figure 7(b) are apparently insensitive to the small hodograph-plane irregularity near AO and thus remain smooth to the eye.

We stress that the termination of $q_v = \text{constant}$ solutions when $M_0 \rightarrow 1$ is due to restrictions on the hodograph-plane formulation. There may perhaps exist nearby

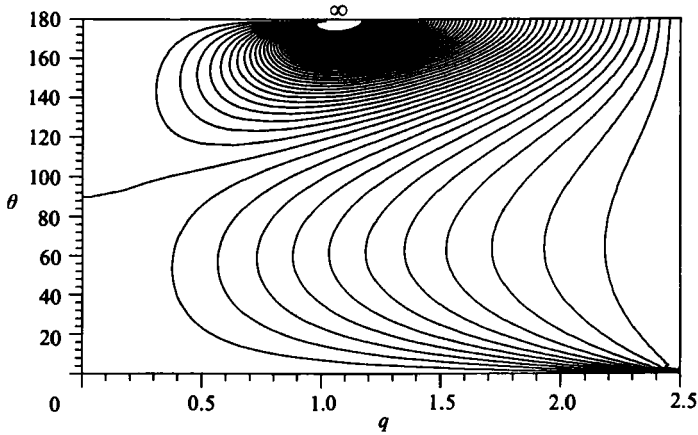


FIGURE 6. Contours of stream function ψ in the (q, θ) -plane, $-8\psi_v \leq \psi \leq \psi_v$, $q_v = 2.5$, $M_\infty = 0.35$. $\psi = 0$ is the stagnation streamline. Equal increments in ψ .

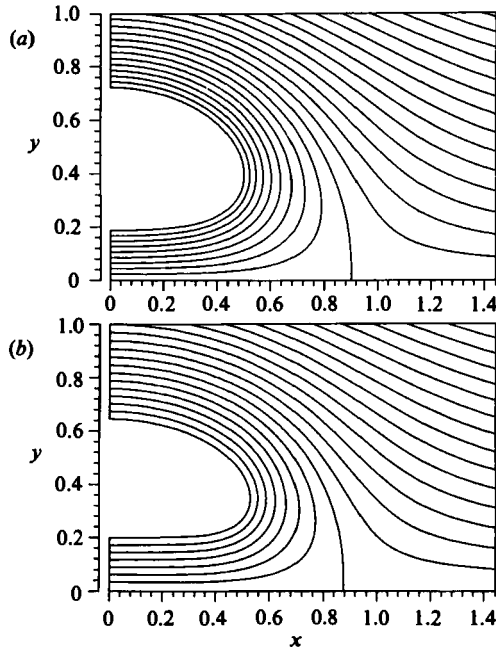


FIGURE 7. Streamlines in the (x, y) -plane. (a) $q_v = 2.5$, $M_\infty = 0$; (b) $q_v = 2.5$, $M_\infty = 0.35$, $M_v = 0.937$, $M_0 = 0.9284$. Equal increments in ψ . $q_\infty = 1$, $\Gamma = 2\pi$.

solutions with $M_0 > 1$, where the vortex boundary develops a waist at A , but if so, these are unobtainable by the present method.

When q_v exceeds about 3, the results summarized in figure 4 and in tables 2-6 indicate the existence, for M_∞ above the $M_v = 1$ curve, of families of continuous solutions corresponding to isentropic shock-free transonic flow. The vortex core is then surrounded by an annulus of supersonic flow outside which the flow is subsonic. Examples of streamlines in the hodograph and physical planes for transonic solutions are shown in figures 8(c), 9(b), 10(c) and 11(b) respectively. Figures 8(c) and 10(c)

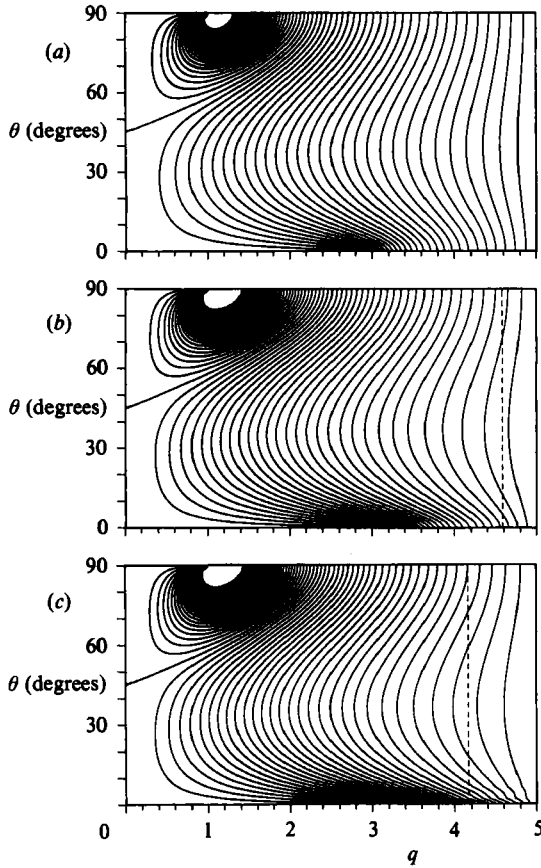


FIGURE 8. Contours of stream function ψ in the (q, θ) -plane, $-1.2\psi_v \leq \psi \leq \psi_v$, $q_v = 5$.
 (a) $M_\infty = 0$, (b) $M_\infty = 0.20$, (c) $M_\infty = 0.22$; ----, sonic line $q = c^*$.

show that a fluid particle which enters the flow domain of figure 1 near A can first undergo a deceleration to a subsonic state, and is thereafter accelerated towards the vortex top near B , to a state which may or may not be supersonic. The sonic lines of figures 9(b) and 11(b) obey Nikolskii & Taganov's theorem (Landau & Lifshitz 1959) requiring a monotonically turning velocity vector, as we move along the sonic line. In figure 9(b) the sonic line appears on the scale drawn to intersect the vertical axis below the vortex at an angle of less than 90° , possibly because of insufficient resolution in the calculation near $\theta = 0$, $q_0 < q \leq q_v$. To support this interpretation, we recall that, in view of (3.1), (3.2) and (3.6), the equation of the sonic line is

$$\frac{dz}{d\theta} = \frac{e^{i\theta}}{\rho(c)} \left(\psi_q + \frac{i}{c} \psi_\theta \right), \quad (5.3)$$

so that, for small θ ,

$$\frac{dy}{d\theta} = \frac{1}{c\rho(c)} \psi_\theta. \quad (5.4)$$

Now it can be seen from figure 8(c) that ψ_θ changes very rapidly from its value 0 on $\theta = 0$ (giving $dy/d\theta = 0$ on $\theta = 0$) to its finite interior values. We have failed to resolve the effect of this transition so that the sonic line appears to have finite slope at $\theta = 0$.

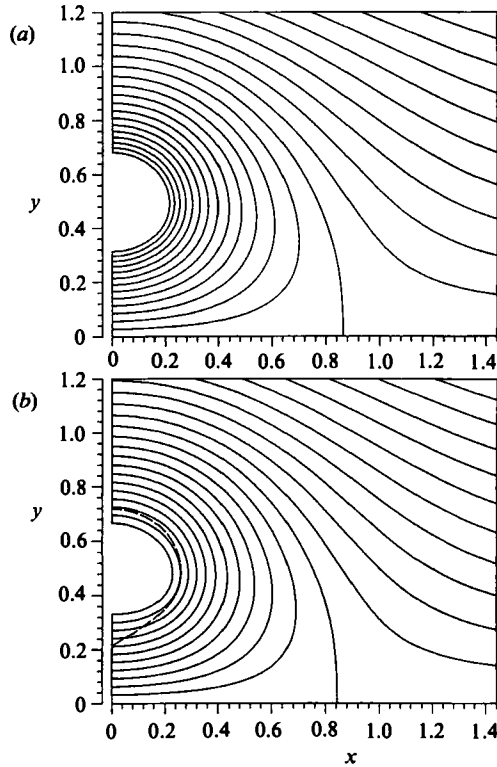


FIGURE 9. Streamlines in the (x, y) -plane. (a) $q_v = 5$, $M_\infty = 0$; (b) $q_v = 5$, $M_\infty = 0.220$, $M_v = 1.255$, $M_0 = 0.798$. Equal increments in ψ . ----, sonic line. $q_\infty = 1$, $\gamma = 2\pi$.

5.4. The appearance of limiting lines

When $q_v = 5$, 10 and 15, solutions with $q_v = \text{constant}$ were found to be terminated not when $M_0 \rightarrow 1$, but by the earlier appearance in the supersonic subdomain of the (q, θ) -plane of regions where $\Delta > 0$ (see (3.10)). This is indicated in figure 4. As was remarked in §3, the occurrence of $\Delta = 0$ in the hodograph plane leads to cuspidal streamlines in the physical plane, and the images of (q, θ) -plane curves where $\Delta = 0$ are called limiting lines (Kuo & Sears 1954). When $\Delta > 0$, which can occur only in the supersonic subdomain, the physical plane becomes multiple valued and the fold is bounded by the limiting lines. The physical significance of the appearance of limiting lines in hodograph solutions of isentropic compressible flow has been much discussed in the literature, mainly in relation to external flow about airfoils (e.g. Garabedian & Korn 1971; Nieuwland & Spee 1973; Sobieczky & Seebass 1984) and to internal nozzle flows. We shall simply take the view that the vanishing of Δ signals the breakdown of the symmetric isentropic potential flow for our model of the compressible vortex pair.

We note in passing that a steady recirculating flow about a vortex containing a compression shock or shocks is not possible since the entropy would not then be a single-valued function of position but would increase, following a particle with each passage through the shock.

Regions of the (q, θ) -plane where $\Delta > 0$ first appeared for $q_v = 5$ at $M_\infty = 0.231$ ($\delta M_\infty = 0.001$) ($J \times I = (76 \times 20)$) and at $M_\infty = 0.225$, ($\delta M_\infty = 0.005$) ($J \times I =$

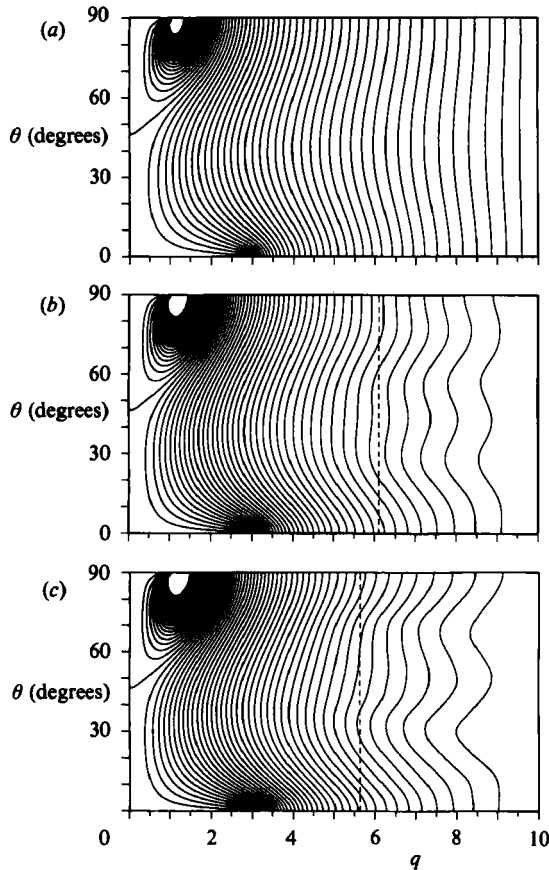


FIGURE 10. Contours of stream function ψ in the (q, θ) -plane, $-0.75\psi_v \leq \psi \leq \psi_v$, $q_v = 10$.
 (a) $M_\infty = 0$; (b) $M_\infty = 0.150$; (c) $M_\infty = 0.1625$. ----, sonic line $q = c^*$.

(150×40), where δM_∞ is the increment in M_∞ . With $q_v = 10$ we found $\Delta > 0$ first at $M_\infty = 0.1625$ ($\delta M_\infty = 0.0025$) for both $(J \times I) = (76 \times 20)$ and (150×40) while when $q_v = 15$, $\Delta > 0$ occurred when $M_\infty = 0.130$ ($\delta M_\infty = 0.005$), $(J \times I) = (150 \times 40)$. These values for $(J \times I) = (150 \times 40)$ are shown in figure 4, and the last entry in each of tables 4 and 5 shows the largest M_∞ for which no regions of $\Delta > 0$ or of $|\Delta| > 1/(4\Delta q_{\min}^2)$ (indicating the possible presence of branch lines when $\Delta \rightarrow \infty$; these were never found) in the (q, θ) -plane were detected. In figure 12 we show contours of ψ and Δ in the (q, θ) -plane which illustrate the onset of $\Delta \geq 0$ as M_∞ is increased at $q_v = 10$. At $M_\infty = 0.150$ streamlines are smooth in the transonic region. When $M_\infty = 0.1625$ the supersonic flow deceleration near the vortex boundary is rapid. This is exacerbated for $M_\infty = 0.1650$ and two regions of $\Delta > 0$ appear, one near $\theta = 30^\circ$ and a tiny, just visible second region near $\theta = 70^\circ$. The vortex boundary shapes corresponding to figures 12(ii) and (iii) are shown in figure 13. At the point marked *C* in figure 13(b) the vortex boundary actually crosses itself on a small scale in a double cuspidal form, as expected.

Although we found no difficulty in obtaining hodograph solutions for M_∞ above the critical value when $\Delta = 0$, no systematic attempt was made to fully search this region of (M_∞, q_v) -space for the possible reappearance of solutions with $\Delta < 0$ everywhere.

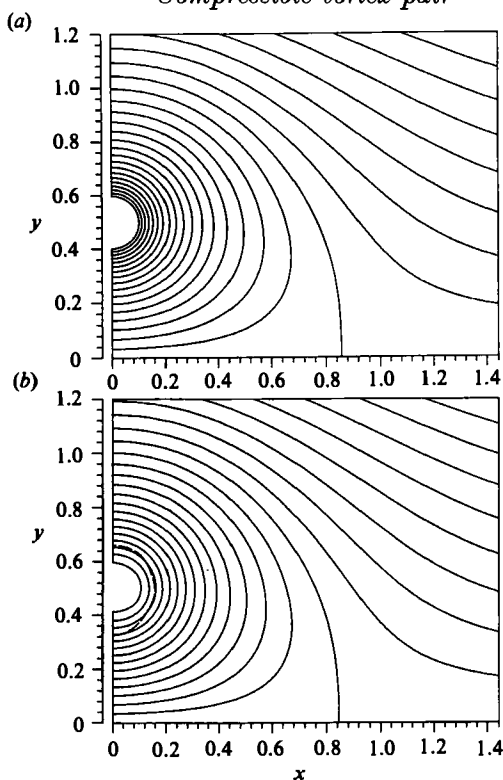


FIGURE 11. Streamlines in the (x, y) -plane. (a) $q_v = 10, M_\infty = 0$; (b) $q_v = 10, M_\infty = 0.150, M_v = 2.014, M_0 = 0.492$. Equal increments in ψ . ----, sonic line. $q_\infty = 1, \gamma = 2\pi$.

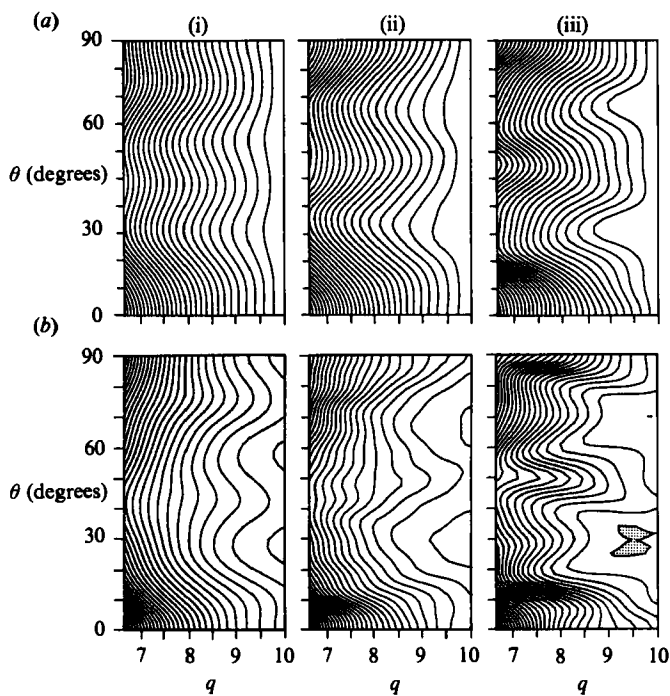


FIGURE 12. (a) contours of ψ in the transonic region of the (q, θ) -plane: (i) $M_\infty = 0.150$; (ii) $M_\infty = 0.1625$; (iii) $M_\infty = 0.1650$. (b) contours of Δ (equation (3.9)) in the (q, θ) -plane. Same q_v, m_∞ as for (a). Shaded region, $\Delta > 0$.

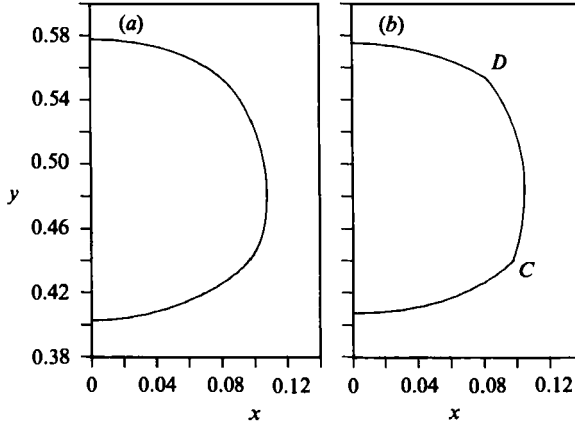


FIGURE 13. Vortex boundary shapes in the physical plane, $q_v = 10$, $q_\infty = 1$, $\Gamma = 2\pi$. (a) $M_\infty = 0.1625$; (b) $M_\infty = 0.1650$; small regions corresponding to $\Delta > 0$ in the (q, θ) -plane are labelled C and D .

We remark that for all calculations reported here, both the eigenvalues and the determinant of the Jacobian of (4.14) were checked to test for possible bifurcations but none were detected. As pointed out earlier we were unable to search for possible bifurcations to solutions with an asymmetric vortex boundary shape owing to the basic symmetry properties built into the solution method.

5.5. The EV results

Having described our results on the CPV we turn to the EV case. The principal physical parameters for the evacuated vortex are summarized in table 7, while the shapes of the half-vortex boundary on which $M_v \rightarrow \infty$ and ρ_v , p_v and $T_v \rightarrow 0$, are shown in figure 14. In table 7 $(ab)^{\frac{1}{2}}$ is a measure of the mean vortex radius \bar{r}_{\min} and $(a*b^*)^{\frac{1}{2}}$ is a measure of the mean radius of the sonic line \bar{r}^* . For isentropic compressible flow about an isolated evacuated vortex $\bar{r}^*/\bar{r}_{\min} = [(\gamma + 1)/(\gamma - 1)]^{\frac{1}{2}}$. There is only one parameter M_∞ for the EV and the procedure followed was to increment M_∞ from the minimum practicable value of $M_\infty = 0.02$ where $q_{ev} = 111.8$, to a value where again regions where $\Delta > 0$ were detected in the (q, θ) -plane. With $(J \times I) = (600 \times 30)$ and (300×40) this occurred at $M_\infty \approx 0.0900$ ($\delta M_\infty = 0.0025$); when $(J \times I) = (150 \times 40)$ (not tabulated), this happened at $M_\infty = 0.0925$ ($\delta M_\infty = 0.0025$). In figure 14 the vortex boundary shapes are only slightly elliptical at $M_\infty = 0.02$. Distortion of the boundary shapes increases with M_∞ until when $M_\infty = 0.0900$ (not shown) the vortex boundary forms, near point C , the self-crossing cuspidal shape characteristic of the physical-plane fold produced when $\Delta > 0$ in the (q, θ) -plane. The increasingly large deviation from a circle of the vortex shape when M_∞ increases is caused by the strain field generated by the presence of the companion vortex. This is analysed in detail in §6 where comparisons between the axis ratios a/b predicted numerically and by the perturbation theory are discussed.

We found no evidence of possible bifurcations of the solution branch in the calculated range of M_∞ , and no suggestion of a return to physically realizable solutions in the range $0.09 \leq M_\infty \leq 0.20$.

$J \times I$	M_∞	q_{ev}	α_q	q_0	ψ_v	D	$(ab)^{\frac{1}{2}}$	$\frac{(a^*b^*)^{\frac{1}{2}}}{(ab)^{\frac{1}{2}}}$	Γ
300×40	0.02	111.8	7.845	3.038	3.3742	0.4990	0.00858	2.539	6.023
600×30			8.020	3.008	3.3826	0.4996	0.00880	2.483	6.186
Asymptotic			—	3.003	3.3766	0.5	0.008944	2.449	2π
300×40	0.04	55.91	6.981	3.033	2.6843	0.4982	0.0175	2.494	6.140
600×30			7.000	3.007	2.6855	0.4984	0.0178	2.465	6.239
Asymptotic			—	3.011	2.6836	0.5	0.01789	2.449	2π
300×40	0.05	44.73	5.923	3.038	2.4613	0.4978	0.0221	2.478	6.193
600×30			—	3.017	2.4605	0.5	0.02236	2.449	2π
Asymptotic			—	—	—	—	—	—	—
300×40	0.06	37.28	5.481	3.044	2.2789	0.4976	0.0266	2.470	6.199
600×30			5.494	3.020	2.2777	0.4973	0.02688	2.446	6.258
Asymptotic			—	3.020	2.2783	0.5	0.02683	2.449	2π
300×40	0.07	31.96	4.937	3.053	2.1247	0.4968	0.0311	2.463	6.191
600×30			—	3.034	2.1243	0.5	0.03129	2.449	2π
Asymptotic			—	—	—	—	—	—	—
300×40	0.08	27.97	4.376	3.065	1.9911	0.4963	0.0357	2.451	6.175
600×30			—	3.045	1.9910	0.5	0.03575	2.449	2π
Asymptotic			—	—	—	—	—	—	—
300×40	0.0850	26.33	4.232	3.073	1.9305	0.4956	0.0380	2.446	6.167
600×30			—	3.051	1.9304	0.5	0.03799	2.449	2π
Asymptotic			—	—	—	—	—	—	—
300×40	0.875	25.57	4.095	3.078	1.9016	0.4955	0.0392	2.441	6.150
600×30			—	3.054	1.9014	0.5	0.03910	2.449	2π
Asymptotic			—	—	—	—	—	—	—

TABLE 7. Calculated properties for the compressible evacuated vortex shown compared to predictions of the leading-order asymptotic theory of Appendix B. $q_\infty = 1, A = -1$.

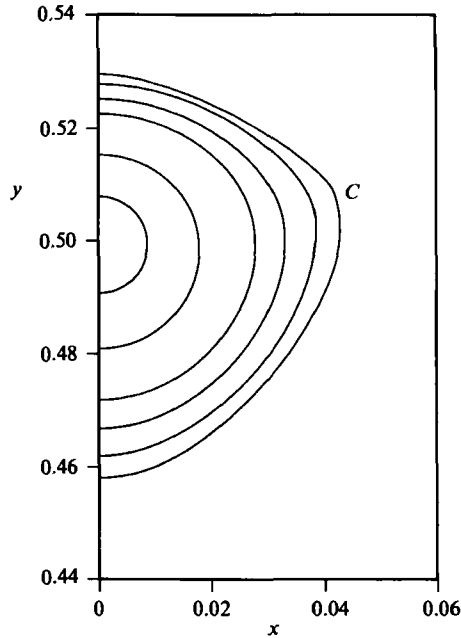


FIGURE 14. Vortex boundary shapes in the physical plane for the evacuated vortex. From centre: $M_\infty = 0.02, 0.04, 0.06, 0.07, 0.08, 0.0875$, limiting lines detected near point C for $M_\infty = 0.090$. $q_\infty = 1, A = -1$.

5.6. Uniqueness

Finally we note that where we obtained numerical solutions with $A < 0$ everywhere, these were smooth functions of M_∞ , suggesting that eigensolutions are not present. Moreover, had the problem been ill posed, the solution would have been sensitive to changes in the mesh size and to changes in ψ_v and q_0 ; this would have been likely to have prevented the Newton iteration from converging. The detailed results presented in tables 1–8 reveal no such sensitivity to J or I , and we can infer lack of sensitivity to ψ_v and q_0 from the convergence of the Newton method. Also for $q_v = 10$, $M_\infty = 0.10$ – 0.160 ($\delta M_\infty = 0.01$) and $M_\infty = 0.1650$ – 0.1750 ($\delta M_\infty = 0.0025$) we have examined the diagonal elements of the LU decomposition of the banded matrix. In particular the ratio of the smallest element to the next smallest was always nearly unity, indicating a non-singular matrix and further strengthening the case against eigensolutions.

6. Approximate theory for $M_\infty \ll 1$

Since the incompressible flow corresponding to $M_\infty = 0$ is known exactly, it must be possible to determine an approximation to the flow for $M_\infty \ll 1$ by the methods of perturbation theory. However, as pointed out by Barsony-Nagy *et al.* (1987, referred to as BN hereinafter) the occurrence of supersonic flow near the vortices renders the perturbation singular and they explain how to overcome this difficulty using matched asymptotic expansions. We shall apply their method to our problem to obtain, in particular, an estimate of the shape of the vortex boundaries.

For this calculation, it is convenient to non-dimensionalize differently, reflecting

the fact that we shall be working in the physical plane. Thus we define a dimensionless complex coordinate z and velocity potential ϕ by

$$D'z = x' + iy' \quad (6.1)$$

and
$$\frac{\Gamma}{2\pi} \phi = \phi'. \quad (6.2)$$

6.1. The far field

First we develop the Rayleigh–Janzen expansion

$$\phi = \phi_0 + M_\infty^2 \phi_1 + \dots, \quad (6.3)$$

where
$$\phi_0 = \text{Re} \{ -i \ln(z-i) + i \ln(z+i) - \frac{1}{2}z \} \quad (6.4)$$

is the incompressible flow for a vortex pair. Substitution of the expansion (6.3) in the governing equation for the velocity potential

$$\nabla^2 \phi = 2M^2 \nabla \phi \cdot \nabla ((\nabla \phi)^2), \quad (6.5)$$

where
$$M(x, y) = \frac{\Gamma}{4\pi D'c'} \quad (6.6)$$

is a local Mach number, leads to

$$\nabla^2 \phi_1 = 2\nabla \phi_0 \cdot \nabla ((\nabla \phi_0)^2). \quad (6.7)$$

We insist that
$$\phi_1 \rightarrow 0 \quad \text{as } |z| \rightarrow \infty \quad (6.8)$$

(and here our procedure differs from BN) and find that the solution of (6.7) satisfying (6.8) is

$$\phi_1 = [2(z^2 + 1)(\bar{z}^2 + 1)]^{-1} \text{Re}((7z - 2z^2\bar{z} + \bar{z}^3). \quad (6.9)$$

This result enables us to calculate the velocity at O and we find

$$\left| \frac{q'_0}{q'_\infty} \right| = 3 + 7M_\infty^2 + O(M_\infty^4), \quad (6.10)$$

which can be used to provide an initial estimate for q_0 for the solution of (2.33) and (2.34) in the evacuated vortex case.

We note in passing that, according to (6.10), $M_0 = 1$ when $M_\infty = 0.281\dots$, confirming how rapidly compressibility effects become important near the vortex pair as M_∞ is increased.

We can see from (6.9) that ϕ_1 is singular at $z = \pm i$ and that ϕ_1 has a worse singularity than ϕ_0 . In fact if we introduce local polar coordinates $(\hat{r}, \hat{\theta})$ defined by

$$z = i + \hat{r} e^{i\hat{\theta}}, \quad (6.11)$$

then, as $\hat{r} \rightarrow 0$ with M_∞ fixed,

$$\phi \sim \hat{\theta} - \frac{1}{8}\hat{r}^2 \sin 2\hat{\theta} + M_\infty^2 \left(\frac{\cos \hat{\theta}}{4\hat{r}} - \frac{3}{4} \sin 2\hat{\theta} \right) + O(M_\infty^4). \quad (6.12)$$

BN remove the \hat{r}^{-1} term by adding to ϕ_1 a complementary function which cancels it, but we prefer to remove it by a small change of origin of our local polar coordinate system. In fact, if we replace (6.11) by

$$z = i(1 - \frac{1}{4}M_\infty^2) + r e^{i\theta}, \quad (6.13)$$

we can show that
$$\phi = \theta - \frac{1}{8}r^2 \sin 2\theta - \frac{3}{4}M_\infty^2 \sin 2\theta + \dots \quad (6.14)$$

The second term in (6.14) is the strain field due to the second vortex and it will emerge that it is responsible for the shape distortion.

6.2. *The near field*

This approximation is valid only so long as compressibility effects are small, so that it applies in the range $M_\infty \ll r \ll 1$ and is the inner form of the outer expansion of ϕ . Thus we must seek a complementary inner approximation valid when $0 \leq r \ll 1$ and insist that the two approximations agree in their common region of validity. It is convenient to put

$$r = sM_\infty \quad (6.15)$$

and seek an expansion of the form

$$\phi = \theta + M_\infty^2 \phi_1(s, \theta) + \dots \quad (6.16)$$

Substitution into (6.5) leads to

$$\left(1 - \frac{2(\gamma-1)}{s^2}\right) \frac{\partial^2 \phi_1}{\partial s^2} + \left(1 - \frac{2(\gamma-3)}{s^2}\right) \frac{1}{s} \frac{\partial \phi_1}{\partial s} + \left(1 - \frac{2(\gamma+1)}{s^2}\right) \frac{\partial^2 \phi_1}{\partial \theta^2} = 0, \quad (6.17)$$

an equation due Taylor (1930). BN show that (6.17) can be integrated in terms of hypergeometric functions, and if

$$\tau = 2(\gamma-1)s^{-2}, \quad (6.18)$$

the general solution with angular dependence $\sin 2\theta$ is

$$\phi_1 = \tau(A\omega_1(\tau) + B\omega_2(\tau)) \sin 2\theta. \quad (6.19)$$

In (6.19),

$$\omega_1(\tau) = F(a, b, 3, \tau) \quad (6.20)$$

is the solution of the hypergeometric equation regular at $\tau = 0$ and ω_2 is the linearly independent singular solution whose behaviour as $\tau \rightarrow 0$ is given by (Abramovitz & Stegun 1970, p. 564)

$$\omega_2(\tau) = \frac{\beta_2}{\tau^2} + \frac{\beta_1}{\tau} + \ln \tau + O(1). \quad (6.21)$$

In (6.20) and (6.21) a and b are given by

$$a = \frac{2\gamma-1 + (4\gamma^2-3)^{\frac{1}{2}}}{2(\gamma-1)},$$

$$b = \frac{2\gamma-1 - (4\gamma^2-3)^{\frac{1}{2}}}{2(\gamma-1)}, \quad (6.22)$$

and

$$\beta_2 = \frac{-2}{(1-a)(2-a)(1-b)a(2-b)} \quad (6.23)$$

and

$$\beta_1 = \frac{2}{(1-a)(1-b)}. \quad (6.24)$$

The asymptotic behaviour (6.21) shows that for $r/M_\infty \gg 1$ the outer form of the inner expansion is

$$\phi = \theta + \left(M_\infty^2 B\beta_1 + \frac{B\beta_2}{2(\gamma-1)} r^2\right) \sin 2\theta + \dots \quad (6.25)$$

Comparing (6.14) and (6.25) shows that the two expressions agree if

$$B\beta_2 = -\frac{1}{4}(\gamma - 1); \quad (6.26)$$

the fact that, with this value of B ,

$$B\beta_1 = -\frac{3}{4} \quad (6.27)$$

is a check of consistency.

6.3. The boundary shape

We next consider how to calculate the shape of the vortex boundary. The unperturbed shape is a circle $\tau = \tau_B$. In view of the θ -dependence of the $O(M_\infty^2)$ terms in ϕ , it is reasonable to suppose that the perturbed shape is

$$\tau = \tau_B + M_\infty^2 D_0 \cos 2\theta + \dots \quad (6.28)$$

The constants A in (6.19) and D_0 are determined by the two requirements that (6.28) is a streamline and that $|\nabla\phi|^2$ is constant on (6.28), both conditions being satisfied to $O(M_\infty^2)$ only. We shall suppress the lengthy algebra involved and give only the final result. Equation (6.28) represents an ellipse with axis a parallel to the flow at ∞ and axis b parallel to the line joining the vortices. Our result is

$$\frac{a}{b} = 1 - \frac{2M_\infty^2 \tau_B^{-1} (1 - \tau_B)^{-1/(\gamma-1)}}{(\tau_B \omega'_1(\tau_B) - \omega_1(\tau_B))} + \dots \quad (6.29)$$

Before we can use (6.29), we must express τ_B in terms of the parameters of the problem and, to leading order,

$$\tau_B = \left(\frac{q'_v}{q'_{ev}} \right)^2. \quad (6.30)$$

The evacuated vortex is thus $\tau_B = 1$, and letting $\tau_B \rightarrow 1$ in (6.29) gives, for $\gamma = 1.4$,

$$\frac{a}{b} = 1 + 25.6 M_\infty^2 + \dots \quad (6.31)$$

Thus the perturbation theory shows that the vortex cores are ellipses, with their major axes parallel to the flow and, in view of (6.13), their centres of vorticity shifted inwards relative to the incompressible far field. Such a shift was shown by BN to occur generally. In our case it implies that the propagation number P defined by

$$P = \frac{4\pi D q_\infty}{\Gamma} \quad (6.32)$$

is given by

$$P = 1 - \frac{1}{4} M_\infty^2 + \dots, \quad (6.33)$$

so that the effect of compressibility is to reduce the speed of the vortex pair.

6.4. Comparison with numerical results

A comparison between our numerical results for the axis ratio and (6.29) is shown in table 8, the limiting form (6.31) being used in the evacuated case. The agreement is good, except for the cases $q_v = 2.5$ and 3.0 where presumably the vortices are too far from the circular (see figure 7) in the incompressible case for perturbation theory to be applicable.

The prediction (6.33) that compressibility slows down the vortex pair agrees poorly with the data, as is clear in table 9. The trend is correctly predicted by (6.33)

$q_v = 2.5$			$q_v = 3$			$q_v = 5$		
M_∞	Num.	Pert.	M_∞	Num.	Pert.	M_∞	Num.	Pert.
0	1.87	1.64	0	1.56	1.44	0	1.17	1.16
0.10	1.90	1.66	0.10	1.59	1.47	0.10	1.20	1.18
0.20	2.00	1.73	0.20	1.68	1.54	0.15	1.24	1.22
0.30	2.39	1.87	0.30	1.92	1.69	0.20	1.31	1.28
$q_v = 10$			$q_v = 20$			Evacuated vortex		
M_∞	Num.	Pert.	M_∞	Num.	Pert.	M_∞	Num.	Pert.
0	1.041	1.040	0	1.011	1.010	0.02	1.010†	1.010
0.05	1.046	1.046	0.05	1.016	1.017	0.04	1.040†	1.041
0.10	1.069	1.069	0.08	1.050	1.052	0.05	1.064	1.064
0.15	1.155	1.155	—	—	—	0.07	1.094†	1.092
—	—	—	—	—	—	0.08	1.172	1.164
—	—	—	—	—	—	0.0875	1.199	1.196

TABLE 8. Axis ratios for vortex core versus M_∞ . Compressible Poeklington vortex; values of q_v shown, $(J \times I) = (150 \times 40)$. Evacuated vortex: $(J \times I) = (300 \times 40)$. † $(J \times I) = (600 \times 30)$. $q_\infty = 1$, $A = -1$.

$q_v = 2.5$			$q_v = 3.0$		
M_∞	Num.	Pert.	M_∞	Num.	Pert.
0	0	0	0	0	0
0.10	0.005	0.0025	0.10	0.005	0.0025
0.20	0.023	0.01	0.20	0.024	0.01
0.30	0.057	0.0225	0.30	0.056	0.0225
$q_v = 5.0$			$q_v = 10.0$		
0	0	0	0	0	0
0.10	0.004	0.0025	0.05	0.0001	0.00063
0.15	0.006	0.0056	0.1	0.0003	0.0025
0.20	0.008	0.01	0.15	-0.0017	0.0056
$q_v = 20$			Evacuated		
0	0	0	0.02	0	0
0.05	0.004	0.00063	0.04	0.011	0.0003
0.08	-0.035	0.0016	0.05	0.0048	0.00053
			0.06	0.0163	0.0009
			0.07	0.0065	0.0011
			0.08	0.0149	0.0015

TABLE 9. Effect of compressibility on propagation number, using finest grid results in each case. Numerical values are $P(0) - P(M_\infty)$ except for the EV where $P(0.02) - P(M_\infty)$ is displayed. Perturbation values obtained from equation (6.33).

when $q_v = 2.5$ and 3.0 but the effect is underestimated. With $q_v = 5.0$ the agreement is better, but at larger q_v the data reveal no clear trend. We suspect that this may be due to errors in the numerical value of D , which is hard to calculate accurately because of the singularity at 0 . The axis ratio is, of course, unaffected by slight errors in the y -coordinate of A .

Finally, we note that eigensolutions in the form of trapped small-amplitude sound waves of elliptical form would correspond to the vanishing of the denominator of (6.29). Numerical evaluation reveals that this denominator is negative for all τ_B when $\gamma = 1.4$, so we have further support for our contention that eigensolutions are not possible for our problem.

7. Conclusions

We have demonstrated by numerical means that vortex pairs with stagnant cores can propagate steadily in a compressible fluid. Moreover, the flow with respect to axes fixed in the pair can be transonic and shock free. However, unlike the case of a rigid symmetric aerofoil for which transonic shock-free flows are isolated (in the sense that they do not persist under small changes of profile for fixed conditions at infinity or small changes in conditions at infinity for a fixed profile (Morawetz 1956, 1957, 1958)) a family of shock-free transonic flows which depend smoothly on the Mach number at infinity, M_∞ , appears to exist for sufficiently small core radii. Of course, the shape of the cores responds to the change in M_∞ , so there is no conflict with Morawetz's results.

This numerical work extends to the fully nonlinear regime the work of BN who showed, using matched asymptotic expansions, that shock-free transonic flows containing evacuated vortices existed.

Qualitatively, a vortex pair of given dimensions and circulation has its speed of propagation reduced and the distortion of its boundary increased by compressibility effects.

For vortices with large cores, limitations of the hodograph method prevented us from entering the transonic regime. For smaller cores, transonic flow occurred, its extent increasing with M_∞ until limit lines appeared.

We have not been able to determine the value of M_∞ at which, for a vortex at given dimensions and circulation, shocks form in the recirculating region. It would be interesting to study this – necessarily unsteady – flow by solving the time-dependent Euler equations numerically.

We are grateful to Professor Barsony-Nagy for permission to use his results prior to their publication.

Appendix A

We define local coordinates in the hodograph plane by

$$\alpha = q - 1, \quad \beta = \theta - \pi. \quad (\text{A } 1)$$

Introducing this change of variable into (2.12) leads to

$$\begin{aligned} \frac{\partial^2 \psi}{\partial \alpha^2} + (1 - M_\infty^2) \frac{\partial^2 \psi}{\partial \beta^2} = & -(2\alpha + \alpha^2) (1 - p_1(1 + \alpha^2)) \frac{\partial^2 \psi}{\partial \alpha^2} \\ & - (1 + \alpha) (p_2 - p_3(1 + \alpha)^2) \frac{\partial \psi}{\partial \alpha} + p_4(2\alpha + \alpha^2) \frac{\partial^2 \psi}{\partial \beta^2}, \quad (\text{A } 2) \end{aligned}$$

where $p_1 = \frac{1}{2}(\gamma - 1)M_\infty^2$, $p_2 = 1 + p_1$, $p_3 = \frac{1}{2}(\gamma - 3)M_\infty^2$ and $p_4 = \frac{1}{2}(\gamma + 1)M_\infty^2$. Near the singularity at $(0, 0)$ (A 2) takes the form

$$\frac{\partial^2 \psi}{\partial \alpha^2} + (1 - M_\infty^2) \frac{\partial^2 \psi}{\partial \beta^2} = 0 \tag{A 3}$$

with
$$\psi'(\alpha, 0) = 0 \quad (\alpha < 0) \tag{A 4}$$

and
$$\frac{\partial \psi}{\partial \beta}(\alpha, 0) = 0 \quad (\alpha > 0). \tag{A 5}$$

We introduce the local polar coordinates (s, δ) defined by

$$s e^{i\delta} = \alpha + \frac{i\beta}{(1 - M_\infty^2)^{\frac{1}{2}}} \tag{A 6}$$

Then possible solutions of (A 3)–(A 5) are of the form

$$\psi = s^{m/2} \cos \frac{1}{2} m \delta, \tag{A 7}$$

where m has integral values. We must appeal to the form of the solution in the physical plane to see that, as described in §2, $m = -1$.

Thus we write $\psi = \psi_0 + \psi_1$, where

$$\psi_0 = A s^{-\frac{1}{2}} \cos \frac{1}{2} \delta, \tag{A 8}$$

so that, on identifying the dominant terms on the right-hand side of (A 2),

$$\frac{\partial^2 \psi_1}{\partial s^2} + \frac{1}{s} \frac{\partial \psi_1}{\partial s} + \frac{1}{s^2} \frac{\partial^2 \psi_1}{\partial \delta^2} = -2\alpha p_5 \frac{\partial^2 \psi_0}{\partial \alpha^2} - (p_2 - p_3) \frac{\partial \psi_0}{\partial \alpha}. \tag{A 9}$$

Here

$$p_5 = 1 - p_1 + \frac{p_4}{1 - M_\infty^2}$$

and the identity

$$\frac{\partial^2 \phi_0}{\partial \alpha^2} = -(1 - M_\infty^2) \frac{\partial^2 \phi_0}{\partial \beta^2} \tag{A 10}$$

has been used to eliminate β -derivatives. The complementary function in (A 9) is

$$B s^{\frac{3}{2}} \cos \frac{1}{2} \delta + O(s^{\frac{5}{2}}) \tag{A 11}$$

and the particular integral is, after some algebra,

$$A s^{\frac{1}{2}} (B_1 \cos \frac{3}{2} \delta + B_2 \cos \frac{7}{2} \delta), \tag{A 12}$$

where

$$B_1 = \frac{3(1 + \frac{1}{2}(\gamma - 1)M_\infty^4)}{8(1 - M_\infty^2)} - \frac{1}{4}(1 - M_\infty^2), \tag{A 13}$$

$$B_2 = \frac{1 + \frac{1}{2}(\gamma - 1)M_\infty^2}{16(1 - M_\infty^2)}. \tag{A 14}$$

Appendix B

In this Appendix we find a leading-order approximation to the value of the stream function at the boundary of the evacuated vortex.

Let r'_1 denote the distance of the point (x', y') from the upper vortex centre $(0, D')$ and r'_2 distance from the lower. Then the incompressible stream function is

$$\psi' = \frac{\rho'_\infty \Gamma}{2\pi} \left\{ -\ln r'_1 + \ln r'_2 - \frac{y'}{2D'} \right\}; \tag{B 1}$$

note that $\psi'(x', 0) = 0$ as in §1. As we have pointed out in §6, this is an outer expansion, valid when

$$r'_1, r'_2 \ll D'M_\infty. \quad (\text{B } 2)$$

When $r'_1 \ll 1$, we can calculate ψ' for the solution for an isolated hollow vortex. Thus

$$\frac{\partial \psi'_1}{\partial r'_1} = -\frac{\Gamma}{2\pi r'_1} \rho'_s \left(1 - \frac{\Gamma^2(\gamma-1)}{8\pi^2 r'^2 c_s'^2} \right)^{\frac{1}{\gamma-1}}, \quad (\text{B } 3)$$

where s denotes stagnation conditions and (2.10) has been used to calculate ρ' . We note that the radius R' of the EV boundary is given by

$$R' = \frac{\Gamma(\gamma-1)^{\frac{1}{2}}}{2\sqrt{2}\pi c_s'} \quad (\text{B } 4)$$

so (B 3) holds for $r'_1 \geq R'$. It follows that

$$\psi' = \frac{\Gamma \rho'_s}{4\pi} \left\{ (1-s)^{\frac{1}{\gamma-1}} \ln s + F(s) - F(1) \right\} + \psi'_v, \quad (\text{B } 5)$$

where

$$F(s) = \frac{1}{\gamma-1} \int_0^s \ln u (1-u)^{\frac{1}{\gamma-1}} du, \quad (\text{B } 6)$$

and where

$$s = R'^2 / r_1'^2. \quad (\text{B } 7)$$

For $r_1 \gg R$, (B 5) gives

$$\psi' = \frac{\Gamma \rho'_s}{2\pi} \left(-\ln r'_1 + \ln R' - \frac{1}{2} F(1) \right) + \psi'_v. \quad (\text{B } 8)$$

Now

$$\rho'_s = \rho'_\infty + O(M_\infty^2), \quad (\text{B } 9)$$

so that, comparing (B 1) and (B 8) in their common region of validity gives

$$\psi'_v = \frac{\Gamma \rho'_\infty}{2\pi} \left\{ \ln \left(\frac{2D'}{R'} \right) - \frac{1}{2} F(1) - \frac{1}{2} \right\}. \quad (\text{B } 10)$$

For $\gamma = 1.4$, $F(1) = -1.6804$, while for $\gamma = 1.667$, $F(1) = -1.2804$.

REFERENCES

- ABRAMOWITZ, M. & STEGUN, A. 1970 *Handbook of Mathematical Functions*, 9th edn. Dover.
- BARSONY-NAGY, A., ER-EL, J. & YUNGSTER, S. 1987 Compressible flow past a contour and stationary vortices. *J. Fluid Mech.* **178**, 367-378.
- BROWN, S. N. 1965 The compressible inviscid leading-edge vortex. *J. Fluid Mech.* **22**, 17-32.
- CHEN, B. & SAFFMAN, P. G. 1980 Numerical evidence for the existence of new types of gravity waves of permanent form on deep water. *Stud. Appl. Maths* **62**, 1-21.
- GARABEDIAN, P. R. & KORN, D. G. 1971 Numerical design of transonic airfoils. In *Numerical Solution of Partial Differential Equations* (ed. B. Hubbard), vol. 2. pp. 253-271. Academic.
- KÜCHEMANN, D. 1978 *The Aerodynamic Design of Aircraft*. Pergamon.
- KUO, Y. H. & SEARS, W. R. 1954 Plane subsonic and transonic potential flows. In *General Theory of High-Speed Aerodynamics, Vol. VI, High Speed Aerodynamics and Jet propulsion* (ed. W. R. Sears), pp. 490-577. Princeton University Press.
- LANDAU, L. D. & LIFSHITZ, E. M. 1959 *Fluid Mechanics*, Pergamon.
- MACK, L. M. 1960 The compressible viscous heat-conducting vortex. *J. Fluid Mech* **8**, 284-292.

- MANDELLA, M., MOON, Y. J. & BERSHADER, D. 1986 Quantitative study of shock-generated compressible vortex flows. In *Shock Waves and Shock Tubes, Proc. Fifteenth Intl Symp on Shock Waves and Shock Tubes, Berkeley, California* (ed. D. Bershader & R. K. Hanson), pp. 471-477. Stanford University Press.
- MARCONI, F. 1984 Supersonic conical separation due to shock vorticity. *AIAA J.* **22**, 1048.
- MILNE-THOMSON, L. 1966 *Theoretical Aerodynamics*. Macmillan.
- MOORE, D. W. 1985 The effect of compressibility on the speed of propagation of a vortex ring. *Proc. R. Soc. Lond. A* **397**, 87-97.
- MORAWETZ, C. S. 1956 On the non-existence of continuous transonic flow past airfoils. I. *Commun. Pure Appl. Maths* **9**, 45-68.
- MORAWETZ, C. S. 1957 On the non-existence of continuous transonic flow past airfoils II. *Commun. Pure Appl. Maths* **10**, 107-131.
- MORAWETZ, C. S. 1958 On the non-existence of continuous transonic flow past airfoils. III. *Commun. Pure Appl. Maths* **11**, 129-144.
- NIEUWLAND, G. Y. & SPREE, B. M. 1973 Transonic airfoils. Recent developments in theory, experiment and design. *Ann. Rev. Fluid Mech.* **5**, 119-150.
- POCKLINGTON, H. C. 1894 The configuration of a pair of equal and opposite hollow straight vortices of finite cross section moving steadily through fluid. *Proc. Camb. Phil. Soc.* **8**, 178-187.
- SOBIECZKY, H. & SEEBASS, A. R. 1984 Supercritical airfoil and wing design. *Ann. Rev. Fluid Mech.* **16**, 337-363.
- TAYLOR, G. I. 1930 Recent work on the flow of compressible fluids. *J. Lond. Math. Soc.* **5**, 224-240.